THESIS

A NOVEL APPROACH FOR CRITICAL BONE DEFECT REPAIR

Submitted by

Adam Schneiderhan

School of Biomedical Engineering

In partial fulfillment of the requirements

For the Degree of Master of Science

Colorado State University

Fort Collins, Colorado

Summer 2022

Master's Committee:

      Advisor: David Prawel

      Ketul Popat
      Bernard Séguin

ABSTRACT

A NOVEL APPROACH FOR CRITICAL BONE DEFECT REPAIR

Critical bone defects are defined as defects that will not naturally heal over a patient's lifetime, even with surgical stabilization. When these occur in the long bones of the axial skeleton (secondary to trauma, tumor resection, etc.), limb-sparing surgery can be performed to avoid amputation of the limb. This procedure typically involves the installation of a steel locking plate over the defect, along with an endoprosthesis or allograft to fill the void of resected bone. Much progress has been made in the natural bone regeneration using tissue engineering (TE) scaffolds in place of these grafts. Porous hydroxyapatite (HAP) is a well-established bone TE scaffold biomaterial but lacks sufficient mechanical strength when fabricated at porosities shown to best induce osteogenesis. To remedy this, polymers such as polycaprolactone (PCL) are often mixed with HAP to fabricate scaffolds with increase load-bearing capacity. However, the addition of PCL makes the scaffold less osteogenic and dramatically slows the degradation rate of the scaffold. This translates into reduced new bone volume where the PCL cannot be remodeled as new bone is formed.

This project involves a pilot clinical trial of a novel method that augments the gold-standard limb-sparing procedure by implanting a 3D printed endoprosthetic "sleeve" device that attaches to the locking fixation plate and contains and protects the brittle HAp scaffold. The PCL sleeve alleviates the dependency on scaffold strength which enables use of the most osteogenic possible biomaterials at ideal porosities to maximize the rate and density of new bone formation. The purpose of the study is to clinically validate the construct design and surgical procedure. Thus far,

pilot limb-sparing surgeries have been performed on 4 client-owned dogs, in which sleeve-scaffold devices were installed in the critical defects caused by the removal of osteosarcomas in distal epiphyseal radii. Recombinant human bone morphogenic protein-2 (rhBMP-2) was added to the scaffolds to further encourage osteogenesis. Mechanical tests were performed on both the sleeves alone and the full construct installed in canine cadaver limbs. Results from this testing demonstrate the sleeve's ability to prevent mechanical failure of the HAp scaffolds. Similarly, no scaffold failure has been observed in clinical trial patients, with some having the device installed for greater than 24 weeks. Additionally, pressureometry and gait analysis confirmed excellent return of limb function in these animals. However, to date, no new bone formation has been observed within the scaffold devices, which has likely been inhibited by anti-cancer treatment. Regardless, results from *ex vivo* testing and the clinical trial validate the construct design and the viability of our novel method for protecting and maintaining brittle bone tissue engineering scaffolds, while aiding in restoration of normal limb function.

TABLE OF CONTENTS

LIST OF TABLES

LIST OF FIGURES

1. Motivation and Scope

1.1. Motivation

Critical bone defects are defined as defects in bone that will not naturally heal over of a patient's lifetime, even with surgical stabilization. When these occur in the long bones of the axial skeleton (secondary to trauma, tumor resection, etc.), limb-sparing surgery can be performed to avoid amputation of the limb. This procedure typically involves the installation of a steel locking plate over the defect, along with an endoprosthesis or allograft to fill the void left by the resected bone. However, endoprostheses and allografts lack the capability to encourage regrowth of bone and complete healing of the defect. Much progress has been made in natural bone regeneration using tissue engineering (TE) scaffolds in place of these grafts. Porous hydroxyapatite (HAP) is a well-established bone TE scaffold biomaterial but lacks sufficient mechanical strength when fabricated at porosities known to best encourage osteogenesis. To remedy this, polymers such as polycaprolactone (PCL) are often used with HAp in the form of composites to fabricate scaffolds with increased load-bearing capacity. However, the addition of PCL makes the scaffold less osteogenic and dramatically slows the degradation rate of the scaffold. This translates to reduced new bone volume where the PCL cannot be remodeled as new bone if formed.

Therefore, there exists a need for alternative solutions that allow for the use of bioreplacable pure HAp scaffolds while ensuring that they remain intact. This project involved the design, production, and implementation of a device to ensure that such a scaffold could remain both immobilized and undamaged *in vivo* for the long periods necessary for healing of critical and super-critical defects.

1.2. Scope

1.2.1. Project

Our method involves the use of a patient-specific 3D printed PCL support sleeve to protect an osteogenic but brittle HAp scaffold. This scaffold, in conjunction with bone morphogenetic protein-2 (rhBMP-2), is expected to encourage bone regrowth over the length of the critical bone defect. The sleeve is designed to stabilize the defect and immobilize the scaffold to keep it from mechanically failing during the period of bone regrowth. A surgical procedure is developed for the installation of the sleeve/scaffold construct using a steel locking late and a patient specific surgical cutting guide. The device is tested both *ex vivo* and *in vivo* with the purpose of discerning its efficacy in protecting the scaffold without inhibiting bone growth or limb function.

1.2.2. Specific Aims

1. Design and 3D print structurally optimized animal-specific endoprostheses consisting of a tissue engineering hydroxyapatite scaffold and polycaprolactone support sleeve in order to augment the locking-plate style limb-sparing surgery.

2. Develop a surgical technique for implementation of the device, practicing in canine cadavers. This includes the design and 3D printing of a patient-specific surgical cutting guide made from polyethylene terephthalate glycol (PETG).

3a. Mechanically evaluate the device for structural performance. This involves mechanical testing of cadaveric canine limbs implanted with the complete, patient-specific device.

3b. Evaluate flow through the hydroxyapatite gyroid osteoconductive scaffold. While cell growth has been commonly evaluated, permeability of this scaffold type is not yet widely researched.

Porosity, permeability and pore size, are evaluated through a combination of micro computed tomography (μCT) and differential pressure measurements during controlled flow.

4. Perform pilot limb sparing of distal radius in client-owned dogs with naturally acquired osteosarcoma and evaluate functional outcomes through pressureometry and gait analysis.

1.3. Hypothesis

I hypothesize that our sleeve device will prevent scaffold structural failure by providing mechanical support, allowing for the use of osteogenic but brittle ceramic scaffolds. It will do this while causing minimal alterations to the current limb-sparing procedure. The efficacy and viability of this device will be determined via mechanical testing, permeability testing, and clinical analysis of the device installed in client-owned canines.

2. Introduction

2.1. Critical Bone Defects

Treatment methods for critical bone defects, which are defined as defects that will not heal spontaneously in patients' lifetimes, are currently being widely studied in the field of orthopedic trauma medicine[1,2]. The loss of the ability to spontaneously heal typically occurs when the defect becomes longer than 50% of the bone's circumference, usually around 2cm in humans[2]. These defects can be secondary to many influences including trauma, infection resulting in bone resection, developmental deformities, or tumor resection[1].

2.1.1. Canine Osteosarcoma

The treatment target for this study is the critical defects caused by the resection of portions of bone in canines with osteosarcoma (OSA) during limb-sparing procedures. OSA is incredibly prevalent among medium to large size dogs, and has been found to be the cause of between 85% and 98% of all primary bone tumors in dogs[3,4]. Commonly, OSA tumors manifest in the appendicular skeleton (between 64-75% of cases) meaning that the long bones of the legs are most frequently affected[4,5]. Common locations include the distal radius, proximal humerus, and distal femur, and of these, the distal radius is associated with the lowest risk of metastasis[6]. Figure 1 shows a radiograph of a resected tumor of the distal radius in a large dog. The first step in treatment is the complete removal of the primary tumor. This ensures that no primary tumor remains. Therefore any cancer that any remaining cancer is in the form of metastasis. Though metastasis may not be detected at the time of diagnosis, progression of microscopic metastases is common, and results in a median survival time of only around 4 months post-surgery[7]. Because of this, surgeries are accompanied by adjuvant chemotherapy, which extends median survival time to 8-12 months post-surgery[5,7].

Figure 1: Resected OSA Tumor of Dog #2

2.2. Limb-Sparing Solutions

There are two methods of tumor removal for dogs with osteosarcoma of the distal radius: Amputation and limb-sparing surgery. The first common method is amputation of the afflicted limb. While this method has certain advantages over limb-sparing procedures (shorter surgery, lower risk of infection, no risk of implant failure), it has not shown to have increased survival rates over limb-sparing procedures with similar adjuvant chemotherapy[4]. Limb sparing procedures are commonly desired over amputation by pet owners, mainly because these limb-sparing procedures result in excellent return of limb function, which is observed in around 80% of patients[8].

2.2.1. Limb Sparing Procedures with Endoprostheses

Nearly all current limb sparing procedures make use of a surgical steel locking fixation plate, which bridges between the remaining radius and the 3rd metacarpal bone[3,4,9,10]. 6-8 locking screws are used to fix the plate to the radius and 8 screws fix it to the metacarpal. The plate is manually bent to fit the desired level of extension of the foot. The plate fixes the joint in place

5

and provides adequate stability for maintenance of limb function. Along with the plate, a device must be inserted to replace the diseased bone and to stabilize the gap. In the simplest design, a metal endoprosthesis, typically made from steel, is attached to the fixation plate to fill the space (Figure 2). This method provides mechanical support, but there is no opportunity for regrowth or vascularization. Many alternatives to steel endoprostheses have been explored in the past two decades with the goal of achieving the best limb function and quality of life for dogs recovering from OSA limb-sparing surgery.
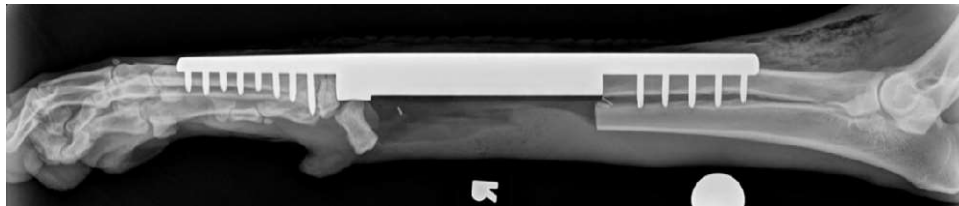
Figure 2: Radiograph of a canine post-limb sparing surgery with a steel endoprosthesis

2.2.2. Autograft, Allograft, Xenograft

There are a few procedures in which the diseased bone is replaced with a graft made from biological bone. The first, in which the tumor is replaced by non-diseased bone from within the patient's body, is called an autograft. This can occur in many forms. A section of the patient's ipsilateral ulna, which is usually remove anyway during the limb spare, can be used to replace the diseased radius[11,12]. Another method involves the pasteurization of the resected tumoral radius. The tumor is removed and then treated with a heat, radiation, or both in order to kill any present cancer cells. The section of bone is then re-inserted into the patient[9,10]. This method has seen some success. Morello et al. reported a median survival time of 324 days among 13 dogs receiving pasteurized tumoral autografts, with 100% of dogs surviving 6 months post-surgery[9].

The second type of graft is an allograft. This refers to a donation to a patient from a non-genetically identical animal of the same species. Allografts are made from cortical bone retrieved

from cadaver canines, and can be matched based on shape, size and side of the affected limb, depending on availability[13]. Liptak et al. performed a study comparing the success of allograft cortical bone to a 316L surgical steel endoprosthesis for OSA limb-sparing surgery, but found no clinically significant difference in surgical and oncological outcome between groups[13].

A third type of graft, a xenograft, in which the donor comes from a different species than the recipient, is commonly referred to as a third category to go with autografts and allografts. However, xenografts are not commonly used in the treatment of osteosarcoma. Compared to autografts and allografts, xenografts carry much more risk of infection, disease, and rejection[14]. Xenografts are instead usually performed in reverse, moving diseased bone from the patient into laboratory mice in order to study the effects of different therapies on living mammals[15].

2.2.3. Shortcomings

While autografts, allografts, and synthetic endoprostheses all have their own advantages, they also have disadvantages. Autografts carry the significant disadvantage of causing donor site trauma. Readily available bone coming from within the patient themselves is in short supply, especially when the grafting of said bone must be healable and tolerable. Using the limited available tissue, such as the ipsilateral ulna, can also result in shortening the total length of the limb[16]. Allografts are the most widely utilized method but have significant shortcomings even beyond the fact that aseptic bone harvesting and storage are quite difficult. The treatments (freezing, autoclaving, radiation, etc.) required to store and sterilized the grafts seem to affect both osteoinduction and mechanical strength[17]. Liptak et al (2006) found no clinical difference between cortical allografts and synthetic endoprostheses, indicating that allografts do very little to integrate into the patient's native bone[13]. Furthermore, allografts can stimulate immune response to donor tissue antigens, which is a common source of complication[18]. Synthetic

7

endoprostheses can be designed with ideal mechanical properties, but, with no real chance of reintegration, fall short of other methods in desirability.

2.3. Osteogenic Tissue Engineering Solutions

Researchers and clinicians study alternative methods that not only spare the limb, but also work towards regeneration of resected bone via tissue engineering (TE). Tissue engineering is a discipline of biomedical engineering which aims towards the restoration, maintenance, or replacement of biological tissue using one or more of the following – material scaffolds, seeded cells, and biological growth factors. In the case of critical bone defect TE, a rigid, porous scaffold is used to fill the defect with the hope that it will encourage the regrowth of native bone. These scaffolds are also designed to naturally degrade, enabling complete replacement by natural bone. The scaffold can either be pre-seeded with stem cells or rely on the body's natural stem cells to penetrate the scaffold and begin growth. Growth factors are also often used to encourage growth or ensure the growth of bone cells specifically.

2.3.1.   Bioceramics as Tissue Engineering Scaffolds

Bioceramics are commonly studied materials for bone tissue engineering because their calcium content and degradability encourage bone regrowth. Calcium phosphate ceramics like hydroxyapatite (HAp) and β-tricalcium phosphate (β-TCP) are used for their favorable levels of bioactivity, biocompatibility, osteoconduction, and angiogenesis[19]. Hydroxyapatite is the primary component in the mineral phase of bone and supports adhesion, growth, and differentiation of osteoblasts while supporting the deposition/substitution of new natural bone[20]. Franch et al. (2020) used a β-TCP scaffold to achieve bridging and union within a 9-12 month period after installation *in vivo* (Figure 3)[21,22]. In fact, HAp and β-TCP scaffolds have been extensively tested both *ex vivo* and *in vivo* with typical results showing excellent bridging and varying levels of

union[21,23–25]. The notable downside of this kind of material is brittleness and inability to sustain the anatomical loads necessary to temporarily replace critical sections of long bone[26]. As a result, pure HAp and pure β-TCP are rarely used, and are almost always employed in the form of composites, with either synthetic or natural polymer additives used to increase compressive strength[23,27,28].
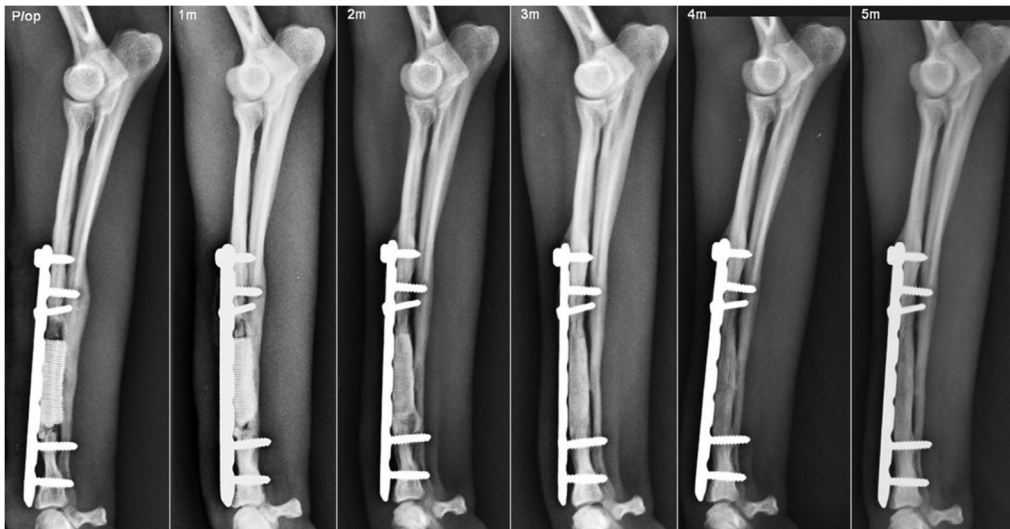
Figure 3: 5 month healing progression of a 2.3cm defect in a Yorkshire terrier using a β-TCP scaffold (Franch et al. 2020)

Polycaprolactone (PCL), a biodegradable and biocompatible polyester is one of the most common additives used for this purpose. However, ceramic-PCL composites have several disadvantages. The increase in strength often comes at the expense of osteoconduction and biodegradability. Although PCL is both biocompatible and biodegradable, these properties do not directly equate to bone growth. While a bioceramic like HAp can be broken down and replaced by bone, PCL must first fully degrade before any bone can grow in the space it occupies. PCL, like most biodegradable polymers, degrades via hydrolysis of its ester bonds, and is absorbed over the course of about 2 years *in vivo*, depending on its molecular weight. This means the addition of PCL to bone TE scaffolds dramatically slows bone growth rate[29]. Surface

modification is also necessary in order to allow any bone growth to occur on PCL because of the hydrophobic nature of the polymer[23]. HAp, conversely, is hydrophilic and naturally encourages cell adhesion and growth. Therefore, it is important to explore methods that allow for the use of pure ceramic scaffolds despite their brittle nature.

2.3.2. Recombinant Human Bone Morphogenetic Protein

Bone Morphogenetic Proteins (BMPs) are multi-functional growth factors belonging to the transforming growth factor beta (TGF-β) superfamily[30]. While approximately 20 BMP family members have been identified and characterized, two (BMP-2 and BMP-7) have the ability to significantly enhance osseointegration and have had forms approved by the FDA for orthopedic disease treatment[31]. These forms are recombinant human BMPs (rhBMP), meaning they are encoded by recombinant DNA in expression vectors, making them widely producible for medical purposes. While rhBMP-2 and rhBMP-7 have both shown very promising results in their ability to achieve healing and union, studies using BMP-2 have tended to yield earlier and quicker healing than those using BMP-7[32,33]. BMP-2 has been used in many osteoinductive therapeutics since it was first identified in the late 1980s[34], including the healing of critical defects in long bones in conjunction with TE scaffolds[23,35–37]. Therefore, BMP-2 was the growth factor of choice for this study.

As is typical, the growth factor's biochemical pathway is quite complex, but in short begins with BMP-2 binding to its transmembrane receptor BMPR2. This allows downstream molecules Smad 1, 5, and 8 to form complexes with Smad4. These complexes are then transported into the nucleus where they can interact with transcription factors that facilitate osteogenesis[30,38]. rhBMP-2 is commonly used in tissue engineering to promote bone growth, and in tandem with HAp TE scaffolds has successfully stimulated bone growth on many occasions[21,23,39–41]. This pairing is so

successful because HAp crystals contain three functional groups with which BMP can interact, the –OH, –NH$_2$, and –COO$^-$ groups[42]. Once BMP is adsorbed onto the HAp matrix of a bone TE scaffold, it can facilitate osteogenesis on site, stimulating osteoblast activity.

The optimal dosage of rhBMP-2 to use in orthopedic surgery is unknown, as previous reports in canines have varied. A project that was able to regenerate and unionize a 2.3cm defect in a Yorkshire terrier used two absorbable collagen sponges (ACS) impregnated with a total of 1.32mg rhBMP-2[21]. Other studies have used much lower quantities of around 0.4mg in canines with nonunion fractures[43]. However, this is a relatively different application involving smaller defects, and is not assumed to be comparable. Other studies report dosage in the form of a fixed concentration of BMP solution (often 0.4-0.5 mg/mL for canines), and saturate either an ACS or compression resistant matrix (CRM) with the solution as their method of delivery[23,44]. It is not known whether different doses are needed between ACS and CRM based on differences in local retention by the materials. This, along with the fact that rhBMP-2 activity can vary from one source to another, implies that best practice is to use the recommendations of the manufacturer when administering BMP during clinical trial. The Infuse Bone Graft Kit (Medtronic, Minneapolis, MN) was used for this project, which has a recommended does of 2mg per patient. It was also determined that a flat, standard dosage between patients would be used to simplify and standardize the surgical procedure.

2.4. Scaffold Geometry

Triply periodic minimal structures (TPMS) are mathematically defined cellular structures with high levels of designability and favorable mechanical properties. Minimal surfaces are defined by their zero-mean curvature, meaning they are equally convex and concave at all points. Being triply-periodic means that they are invariant along three independent directions[45]. This

organization and repeatability make them suitable for additive manufacturing, and they can be

adjusted to obtain ideal porosity and pore size for a given application[46]. In addition, their highly

ordered and interconnected pores, high surface area to volume ratio, and light weight all lend

them towards the ability to mimic trabecular bone[47]. All these features have led to the bloom of

research surrounding the use of TPMS structures as bone TE scaffolds. Gyroids (Figure 4), a

type of TPMS often used in additive manufacturing, have favorable mechanical properties for

bone tissue engineering.
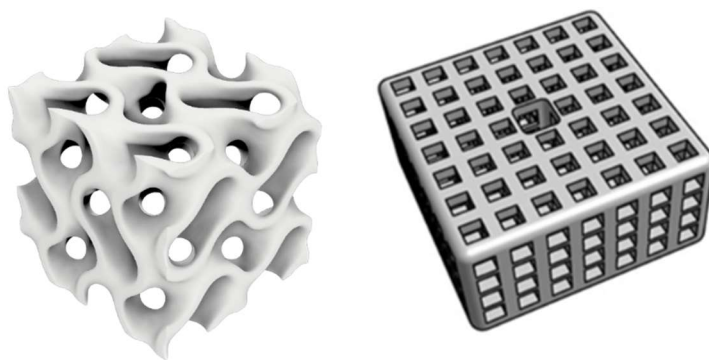
Figure 4: An example of (Left) gyroid morphology and (Right) rectilinear morphology (Ritz et al. 2017)[48]

Gyroids are stiffer and stronger than traditional rectilinear scaffolds, and have relatively high

mechanical energy absorption when compared to other TPMS structures[49,50]. This means that

they have lower likelihood to fail under anatomical load than a rectilinear scaffold of the same

material. Rectilinear scaffolds (Figure 4) are quite popular for bone tissue engineering scaffolds

because they are simpler and often faster to produce. However, they are structurally much

weaker than gyroids, and contain harsher angles that are not conducive to cell growth. Gyroids

made from HAp have been shown to exhibit self-reinforcing behavior after initial failure during

compressive testing[26]. A gyroid scaffold of this type can therefore maintain a similar modulus

after its initial failure. Furthermore, gyroids with controlled porosity and pore size have shown to

be excellent growth environments, with good cell survival and distribution in *in vitro* studies[51]. This compounding of favorable characteristics led to the use of gyroid scaffolds for this study.

2.5. Mechanical Properties of Surgical Implants

Certain mechanical properties are important to consider for this project, both for the individual parts and for the whole construct. Purely ceramic scaffolds are notably brittle, having the tendency to fracture when subjected to stress and very little tendency to deform (low ductility). This is the case with most non-metallic inorganic materials. Conversely, these materials have very low toughness, which is the ability to absorb energy and deform significantly without rupture (resistance to fracture). Tough materials are characterized by high compressive and tensile strength, and while brittle materials typically have high compressive strength, they have very low tensile strength[52]. Because of this low tensile strength and low ductility of the scaffold, the full construct for this project should have a high bending stiffness, and therefore be able to resist/prevent high deformation that could cause scaffold failure. Stiffness is a measure of how much something will deflect under a given load. The amount of device deflection that occurs under physiological load is examined in this study. Along with reducing deformation, the sleeve/plate portion of the construct will also serve to protect the scaffold from impact and to absorb energy that would otherwise be inflicted on the scaffold.

2.6. Permeability of Bone TE Scaffolds

Measuring permeability is a way to quantifiably determine a material's ability to conduct fluid and is dependent on many properties including porosity, pore shape and size, and interconnectivity[53,54]. This is an essential consideration when determining how a material can encourage bone regrowth. Higher permeability values have been shown to correlate to better bone regeneration, which is thought to be because high permeability allows for better nutrient

diffusion, vessel formation, and waste removal[55]. Because bone is a vascularized tissue, vessel formation is also key for viable bone regeneration. In fact, insufficient permeability can cause cartilaginous tissue, which is avascular, to grow instead of bone tissue[54]. However, because permeability increases with pore size, one must find a delicate balance between permeability and mechanical strength[56,57]. A porosity of roughly 70% was chosen for this study because it has become a standard in the field of bone tissue engineering[57–59].

Gyroids have been shown to provide better accessibility to permeating fluid compared to other porous morphologies[53,60]. Their continuous and interconnected pores enables excellent permeability throughout their structure, and while interconnectivity, porosity, and pore size remain the prevalent factors in assessing permeability, these properties are now being supplemented by considerations such as tortuosity and surface area to volume ratio[61]. Gyroids have desirable characteristics in both categories. Tortuosity values correspond to how complex or tortuous a fluid's path through a medium is based on its topology, and a high surface area to volume ratio is favorable for greater cell seeding and growth ability[57,62]. It was therefore predicted that 70% porous gyroid would be the ideal porosity and topology for bone TE scaffold in this study.

The permeability of the gyroid scaffolds in this study will be compared to the permeability of trabecular bone ($0.4\text{-}11\times10^{-9}\text{m}^2$) to assure that they possess sufficient permeability for the flow of interstitial fluid and nutrients for revascularization and bone regrowth[63]. While permeability of TPMS structures is more commonly assessed via computational fluid dynamics (CFD), there remains a consistent error between computational and empirical data, due to factors that CFD models do not account for such as inaccuracies inherent in additive manufacturing and the hydrophobicity of different materials[47,64].

2.7. Additive Manufacturing of Colloidal Ceramic Systems via Photocasting

Additive manufacturing, commonly referred to as 3D printing, has emerged as a popular method for the assembly of bioceramic bon scaffods. This method involves the layer-wise deposition of material for the purpose of forming precise topologies. In order to employ this method for ceramics, high volume-fraction colloidal ceramic slurries are necessary to achieve low microporosity and high strength in the final product. However, the high volume-fraction of ceramic particles results in relatively high viscosity in the colloidal slurry[65]. Previously, a method for the preparation of such a slurry has been described, and printed via a technique referred to as photocasting[26,66]. This method, a combination of robocasting and layer-wise photopolymerization, makes use of a monomer and photoinitiator within the slurry to allow the curing of printed layers as they are extruded[26]. Photocasting enables the printing of complex structures such as gyroids with controlled porosity and pore size ideal for bone tissue engineering.

2.8. Polycaprolactone in Tissue Engineering and Surgical Implants

As previously mentioned, PCL is a biocompatible polyester that is approved by the FDA for numerous uses as implantable biomaterials. With the emergence of the field of tissue engineering in the early 21st century, scholarly interest in PCL saw a surge due to the material's superior rheological and viscoelastic properties[67,68]. This explosion of interest can best be seen in the tripling of PCL-related publications between 2000 and 2010[68]. These superior properties allow for the construction of a wide range of PCL structures[69–71]. Notably, PCL 3D printing through melt extrusion has emerged as a method of making both solid and porous PCL components[72]. This method allows for the creation of complex PCL structures designed using CAD modeling

15

and is an excellent method of production for implantable components meant to degrade over time within the body.

The PCL degradation process is of specific interest to this project. Biodegradable surgical implants and endoprostheses are highly desirable, as they do not need to be removed in subsequent invasive procedures, reducing downstream care as they degrade and naturally exit the body[73]. As an ester-containing polymer, PCL is susceptible to degradation via hydrolysis which, in a physiological environment, is driven via oxidative, enzymatic, and pH-related factors[67]. Once the molecular weight (MW) of the polymer has dropped below 10,000, its fragments enter the cells, where they are completely digested[74]. This means that mass loss does not occur until the polymer chains are allowed to degrade below this point. Sun et al.[73] performed a study in which *in vivo* implants of 66kDa PCL in rats degraded down to 8kDa in 30 months, while Pitt et al.[75] performed a study involving 50kDa implants degrading in rabbits, in which mass loss occurred in the 15-18 month range, when the average MW dropped from 13kDa to 8kDa. More importantly, these studies were able to illustrate that MW would degrade following a logarithmic trend versus linear time[73,75], indicating a first order rate law for the hydrolysis of the ester bonds of PCL[67]. Notably, degradation via hydrolysis means degradation primarily in the bulk of the polymer, not just of the surface[67,76]. This essentially means that a PCL implant will retain its shape and volume much longer than other materials which degrade from the surface and shrink over time. PCL will, however, lose some strength prior to dipping below the 10kDa threshold. Sun et al.[73] found that mechanical strength was maintained when the implants had degraded to 24kDa after 16 months, but had begun to fall at 15kDa and 24 months. This means that we can expect the 80kDa PCL used to create this project's implant (comparing to the 66kDa implants in Sun et al.) to maintain its mechanical strength for longer than 2 years before gradually declining.

16

2.9. A Novel Augmentation of the Limb-Sparing Procedure

2.9.1. Application

The treatment examined in this project is designed for epiphyseal defects in canine distal radii caused by the removal of osteosarcoma. These defects can result in the removal of over half of the radius, and therefore require large endoprostheses and strong mechanical support. This trial was limited to patients with tumors manifesting at the distal radius. The distal radius is associated with a lower risk of metastasis, and canines are well capable of tolerating the necessary arthrodesis of the radiocarpal joint[4,6].

2.9.2. Treatment

Our novel approach to the repair of critical bone defects in this project involves the use of a patient-specific construct comprised of three primary components (Figure 5). The first component is the gold-standard of limb sparing surgery, the steel locking-screw fixation plate. In our and the gold-standard procedure, this plate is fixed to the radius on the proximal end and the third metacarpal on the distal end using locking plate screws. A major goal of the device is that it is an enhancement or augmentation, not an alteration, of the existing limb-sparing procedure. It is therefore designed to fit around the metal fixation plate, and no alteration to the way in which the osteotomy or plate installation are performed occurs. The second component is a gyroid scaffold. The scaffold is pure HAp with 70% porosity, which is ideal for this type of procedure as described earlier. This component is 3D printed via photocasting and is designed to be patient specific, matching the shape of the patient radius and fitting to the exact size of the defect. The scaffold contains a central canal in its core, into which an absorbent collagen sponge (ACS) is placed and then loaded with rhBMP-2 (refer to *Methods* Section 3.6.3 below). This combination of HAp gyroid and rhBMP-2 is predicted to be very favorable for bone growth because it

provides an excellent growth surface, a simulating growth factor, and is completely bioreplacable. However, because the scaffold is purely ceramic rather and a more structurally trustworthy composite, a third component is needed to stabilize and immobilize it. This is accomplished with a 3D printed, patient specific PCL support sleeve. This sleeve covers the length of the scaffold, extending from the proximal end where it overlaps with the radius. At the distal end, the sleeve ends flush with the scaffold so it can maintain bony contact with the radial carpal with the end goal of unionizing with that bone to achieve arthrodesis of the radiocarpal joint, as is standard in limb-sparing surgery.
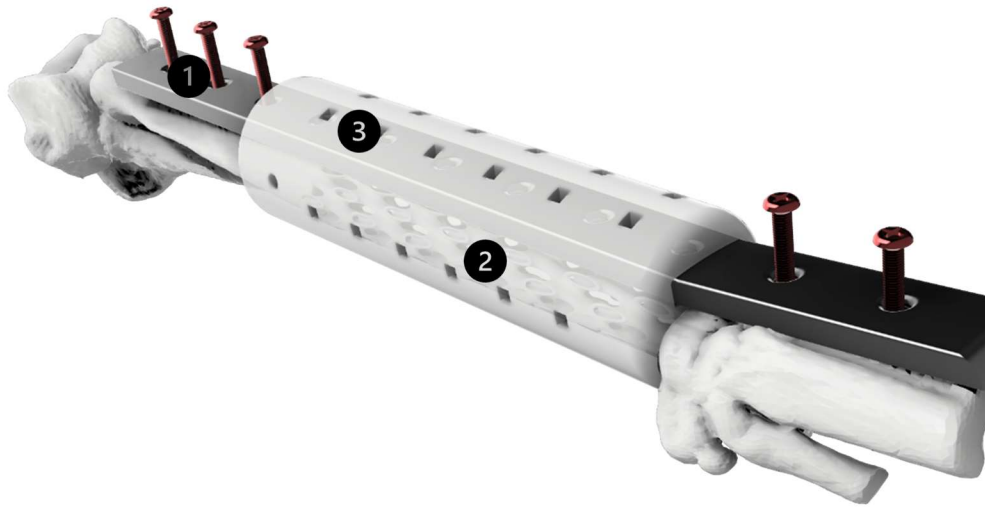
Figure 5: 3D CAD rendering of the full limb-sparing/TE construct as it would be applied to a canine forelimb. The (1) locking fixation plate and (2) osteogenic scaffold slide into the (3) PCL support sleeve, which has been made slightly transparent.

3. Materials and Methods

3.1. Modeling

Each device is modeled based on patient-specific imaging once it is determined that they qualify for the study. This imaging is converted to a 3D mesh to inform the designs for the scaffold, sleeve, and surgical cutting guide. A complete workflow chart for the modeling and preparation of components is available in Appendix E.

3.1.1. Processing of DICOM Data

Unprocessed computed tomography (CT) Digital Imaging and Communications in Medicine (DICOM) data were converted into .stl files to inform the design of each device. The DICOM data was first uploaded to Invesalius (CTI, Brazil) to reconstruct CT data into .stl files to be used for prototyping[77]. In this software, the CT images were segmented and 3D surfaces of the bones were created through application of an image density bone mask. These 3D surfaces were then exported to Autodesk Meshmixer (Autodesk, San Rafael, CA), where all extraneous particles were removed. These particles could occur when the density mask created surfaces from noise in the CT images, resulting in small particles not associated with the skeletal structure. Meshmixer was also used to smooth all surfaces. Bones unnecessary for design of the device such as the humerus and lower metacarpals were also removed from the model. Because the desired final fixated angle of the foot typically differed from the angle at which the CT was taken, the manus of the patient was also dictated in Meshmixer to a 10-degree angle before being exported as an .stl file.

3.1.2. Bioceramic Tissue Engineering Scaffold

CAD modeling of the bioceramic scaffolds was performed in Autodesk Fusion 360 (Autodesk). Scaffold models were parameterized to replace the distal approximately 40% of the length of the

dog's radius. This length could change at the discretion of surgeon depending on the size and shape of the tumor. The proximal end of the scaffold was shaped to match the geometry of the radius at the location of the proximal cut. This shape was lofted to the distal end to make a frustum-like model that could approximate the shape of the resected bone. The distal face of the scaffold is parallel to the proximal face and meets flush with the distal cut to the top of the radial carpal and ulnar carpal bones. Scaffold models were exported to Ultimaker Cura 4.9.1 for slicing in preparation for 3D printing. This allowed for the creation of a 3D printing code file that instructed the printer to print the shape of the model with a gyroid infill at 70% porosity. This porosity is referred to as *designed* porosity, because inaccuracies in the printing process cause slight changes in true porosity. To achieve a purely gyroid structure, the models were sliced with zero top or bottom layers and zero perimeters. A layer height of 0.2mm was used to cooperate with the width of the extrusion needle. Scaffolds were uniformly scaled up by 21% for as-printed dimensions to account for the shrinkage that occurs during sintering due to calcination and the burning off of organic compounds (refer to the 3D printing and sintering method sections below).

3.1.3. PCL Support Sleeve

The PCL support sleeve was designed using Autodesk Fusion 360 (Autodesk). The sleeve is designed to provide mechanical support and impact protection to a highly osteogenic but brittle tissue engineering scaffold. It also serves to immobilize the scaffold and direct flow of nutrients along the length of the scaffold. To ensure that the inner sleeve fit tightly to the patient radius and scaffold, Boolean operations were performed between the 3D DICOM model of the patient's radius and the model of the patient's scaffold. A section was then cut through the sleeve so that it could easily but tightly slide over the metal fixation plate. 10% XY tolerance was added to the

area of the sleeve surrounding the radius to maintain tight contact with the host bone, while 7.5% tolerance was added to the area of the sleeve surrounding the scaffold to immobilize the scaffold and minimize compression damage to the brittle scaffold during insertion into the sleeve. The channel for the plate was sized up uniformly by 1mm to ensure that the plate would fit and to allow for a light bend of the plate at the distal end, and to avoid damaging the scaffold when the plate is inserted into the sleeve during the surgical procedure. At the proximal end of the sleeve, which overlaps the radius, two screw holes were added for fixation of the sleeve to the bone. These holes are countersunk so the head of the screw fits flush with the outer surface of the sleeve. The purpose of the screws is to anchor the sleeve through cis layer of cortical bone each and avoid the plate screws that already run through the radius. 5mm square pores were added throughout the sleeve to enable cross cortical flow but were kept small so that flow would primarily be directed along the length of the inner sleeve.

3.1.4. Surgical Cutting Guide

The surgical cutting guide is necessary to allow the surgeon to resect the correct portion of the radius matching to exactly the length of the scaffold. Cutting guides were designed in Fusion 360. Boolean operations were performed between each cutting guide and a 3D render of the corresponding patient's lower leg skeleton (obtained via CT as described above) so that the guide fit precisely over the area, contacting the distal radius, ulnar head, and 3rd and 5th metacarpals (Figure 6).
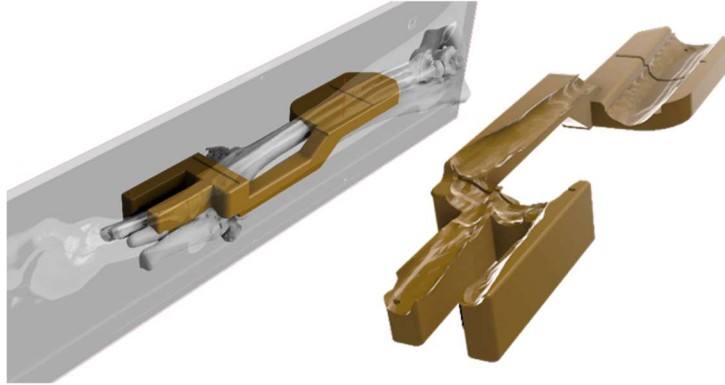
Figure 6: Surgical cutting guide fit to a patient model (left) and displaying the contact area (right)

3.2. Methods for Scaffold Preparation

3.2.1. Slurry Preparation

41 vol% HAp photopolymer resin was synthesized using a planetary ball mill (Across International, Livingston, NJ PQ0NO4) and PTFE milling jars (Across International). Ethylene glycol dimethacrylate (EGDMA) monomer (TCI, Tokyo, Japan) was added along with appropriate amounts of diphenyl (2,4,6-trimethylbenzoyl) phosphine oxide (TPO) photoinitiator and Solplus D540 (Lubrizol, Wickliffe, OH) dispersant and milled for 30 minutes to mix. Hydroxyapatite powder of particle size 85.74±35.72nm (VWR, Radnor, PA) was milled into the mixture in 3 steps of 2hrs, 2hrs, and 4hrs at 300, 320, and 360rpm, respectively. The masses of HAp powder added at each step were 10g, 5g, and 4.31g, respectively, for a total of 19.31g HAp added. This resulted in 15mL batches of 41 %vol HAp photopolymer printing slurry. Rheological properties of the printing slurry were previously verified to have ideal qualities for viscous extrusion-based additive manufacturing[78].

3.2.2. Production of Bone TE Scaffold

Hydroxyapatite bone tissue engineering scaffolds were synthesized via viscous extrusion and photopolymerization of the printing slurry using the Hyrel Engine SR 3D printer (Hyrel 3D,

22

Norcross, GA), equipped with an EMO-XT 15cc reservoir printhead (Hyrel 3D). The printhead was fitted with a 22 gauge luer-lock dispensing tip (Jensen Global, Santa Barbara, CA). This tip was blacked out with a black permanent marker and covered with tape to ensure that light did not cause polymerization of the slurry and clog of the tip. The printhead was equipped with a 405nm low-power LED array (light power density ranging from 0.7 mW/cm^2 to 1.3 mW/cm^2) (Hyrel 3D) which was used to activate the TPO, starting the photopolymerization reaction. Deposited roads were continuously exposed to 405nm light to achieve layer-wise polymerization. Scaffolds were printed onto the room temperature bed of the Hyrel printer, which was covered with blue painter's tape to improve bed adhesion. To reduce the chance of printing failure, longer scaffolds were segmented into pieces no taller than 5cm. Around 4 pieces were typically necessary, depending on the necessary resection size for each patient.

3.2.3. Calcination/Sintering

Sintering is the process in which ceramic particles are consolidated and the scaffold is densified through a high-temperature controlled heating profile. This process serves as a method for removing all organic compounds, mainly PEGDMA, from the scaffold, so that the resulting scaffold is purely HAp. Scaffolds were sintered in a Thermolyne muffle furnace (Thermo Fisher Scientific, Waltham, MA), ramping from room temp by 5°C/min until reaching 1200°C, at which point that temperature was held for 180 minutes. The furnace was then allowed to cool naturally overnight. Scaffolds were placed standing upright in the direct center of the furnace to prevent curvature, which occurred on occasion when once side of the scaffold was heated faster than the other.

3.3. Manufacturing of other Surgical Components

3.3.1. Additive Manufacturing of Support Sleeve

The PCL sleeves were sliced in preparation for 3D printing using Prusa Slicer 2.4 (PRUSA 3D, Prague, Czech Republic). They were manufactured via melt extrusion. Facilan^{TM} OrthoNatural 80kDa PCL filament (3D4Makers, Haarlem, Netherlands) was printed layer-wise using the PRUSA I3 MK3S (PRUSA 3D). PCL was printed at 100% infill with a layer height of 0.2mm. The initial layer was printed onto Ultimaker 2+/3 adhesion sheets (Ultimaker, Utrecht, Netherlands), and all layers were printed at speeds between 20 and 50mm/s. Nozzle temperature was set to 120°C and bed temperature was set to 35°C. Two Prusa print fans were mounted on the head of the printer, with fan speeds held at 100% speed for the duration of the print. Small PCL plugs, designed to prevent ectopic bone formation through the non-utilized screw-holes of the plate, were designed in Fusion 360 and fabricated via the same print settings as the sleeves.

3.3.2. Fabrication of the Surgical Cutting Guide

Surgical cutting guide models were sliced in the Prusa Slicer 2.4 (PRUSA 3D). They were 3D printed via melt extrusion using MH Build Series PETG Filament (MatterHackers, Lake Forest, CA) on the PRUSA I3 MK3S (Prusa 3D). Initial layers were printed onto the same Ultimaker 2+/3 adhesion sheets. Cutting guides were printed at 30% gyroid infill with at least 3 inner perimeters to be able to withstand slightly more impact from surgical tools. They were printed with 0.2mm layer heights with a nozzle temperature of 235°C and a plate temperature of 80°C.

3.4. Sterilization of Surgical Components

Each component of the device was sterilized the day prior to surgery. HAp scaffolds were autoclaved at 121°C and 2 atm for 20 minutes. The PETG cutting guide was sterilized via low-temperature hydrogen peroxide biodecontamination using the Steris Model VHP MD140X

(Steris Life Sciences, Mentor, OH) set to the Lumen cycle. PCL is unable to withstand the heat of an autoclave and has not been tested with hydrogen peroxide biodecontamination, so PCL components (the sleeve and plate plugs) were sterilized by soaking peracetic acid (2500ppm in 20% ethanol)[79]. The sleeve was then rinsed with 2 liters 0.9% saline solution.

3.5. Pre-Clinical Characterization of Device

Characterization of the full construct (scaffold + sleeve + plate) was split into two major aims. The first aim was to ensure that sufficient flow was possible within the osteogenic scaffold, enabling the penetration of the cells and nutrients necessary for bone growth. This was tested via the experimental determination of the permeability of the scaffolds. The second aim was to mechanically characterize the device to ensure that its presence did not reduce stiffness or negatively effect outcomes in comparison to the gold standard limb-sparing procedure. Testing of the preliminary device also provides a basis for comparison to post clinical trial testing, which will indicate how bone growth has affected mechanical behavior of the limbs.

3.5.1. Permeability

An apparatus was developed to determine the permeability of the endoprosthesis by measuring pressure differential across a scaffold during fluid flow. This pressure difference was used with Darcy's law to calculate a permeability value. Darcy's law is shown as follows:

$$-\frac{dP}{dx} = \frac{\mu}{k} \times v$$

where μ is the dynamic viscosity of the fluid (0.001 Pa*s for water at 20°C), v is the linear fluid flow velocity, and k is the Darcian permeability. Darcy's law was chosen to be an adequate approach for this project, given that it is widely used for the calculation of permeability of

25

porous scaffolds such as this[53,54,80]. The equation was rearranged to the following for simpler calculation of permeability values:

$$k = \frac{Q\mu L}{A\Delta P}$$

Where Q is the volumetric flow rate, L is the length of the scaffold, and A is the cross-sectional area of the scaffold. Because Darcy's law assumes laminar flow, it was necessary to characterize the flow through the scaffold. This could be characterized using the Reynolds number, which was calculated using the equation:

$$Re = \frac{\rho v D}{\mu}$$

where ρ is the density of the fluid (997 kg/m^3 for water at 20°C) and D is the mean pore diameter of the scaffold[53].

The device, shown in Figure 7, uses a Validyne P55D transducer (Validyne Engineering, Los Angeles, CA) with an internal membrane that flexes based on differential pressure on either side. Based on this flex, a voltage value is output by the transducer and read by a National Instruments USB-6218 multiofunction I/O device (National Instruments, Austin, TX). Voltage values were then translated to pressure differential via a standard curve. The standard curve was developed via construction of a manometer, as described by the manufacturer (Appendix C). This involved a piece of clear plastic tubing bent into a U-shape and partially filled with water. The difference in the height of water on either side of the "U" shape was measured to determine the pressure in cmH$_2$O, which was converted to Pascals. To create a standard curve, voltage was measured at known water column heights of 5, 10, 15, 20, 25, 30, and 40cm on either side of the transducer.
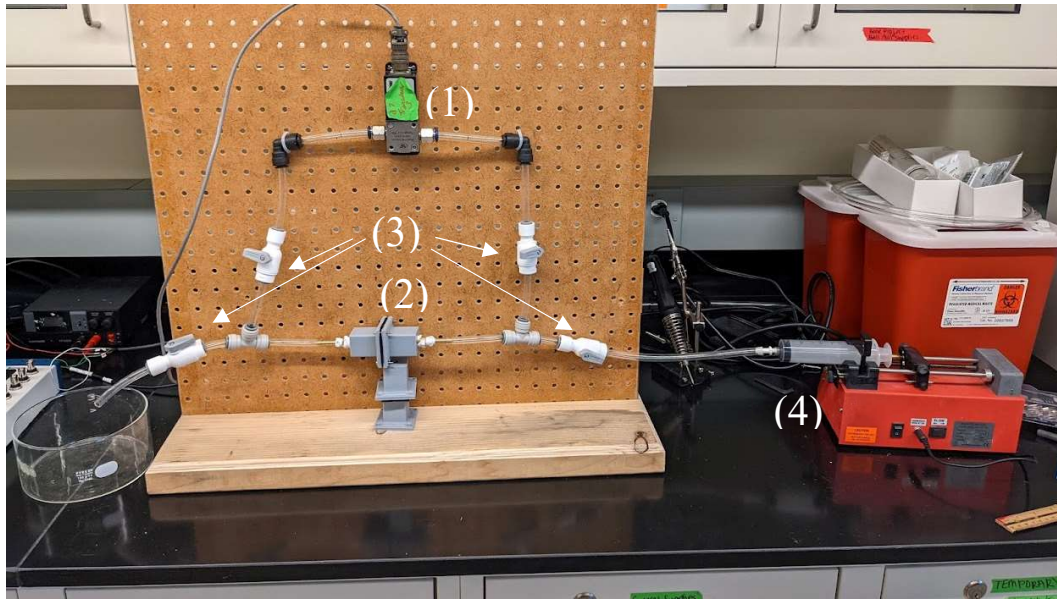
Figure 7: Permeability testing apparatus including the (1) differential pressure transducer, (2) sample chamber, (3) on/off valves, and (4) syringe pump

Six 1cm x 1cm 70% porous gyroid HAp scaffolds of two different lengths (2cm and 3cm) were loaded into customized 3D printed PETG chambers. These chambers were designed in CAD to snugly fit the scaffold while minimizing void space, with a 1x1cm inner chamber lined with Neoprene high-density waterproof sealing foam for waterproofing. Chambers were printed via melt extrusion on the PRUSA I3 MK3S and MH build series PETG filament. They were printed with 10 perimeters to ensure that water would not escape the chamber. Screw and washer holes were added to the corner of the chamber so the two halves could be tightly screwed together. More waterproofing foam is compressed between the two halves to create a fully water-tight chamber. Filtered water was pumped through the system using a 50mL plastic syringe and a Genie Plus syringe pump (Kent Scientific, Torrington, CT). Fluid was pumped at 10, 20, 30, 40, and 50mL/hr to demonstrate how permeability changed with flow rate. Empty chambers were also tested at each flow rate, and the resulting values were subtracted from final values to

account for any natural pressure differential across empty chambers and standardize the experimental data. The flow rates and corresponding to Reynold's numbers are listed in Table 1.

Table 1: Reynolds number values for each flow rate tested in the permeability apparatus. Laminar flow is associated with Reynolds numbers below 2300.

Flow Rate (mL/min)	Flow Rate (m^3/s)	Velocity (m/s)	Reynolds Number
10	2e-07	0.17	116
20	3e-07	0.33	233
30	5e-07	0.50	349
40	7e-07	0.67	465
50	8e-07	0.83	582

3.5.2. Micro-Scale Computed Tomography

Micro-computed tomography (μCT) imaging was performed using a Scanco 80 (Scanco Medical AG, Bruttisellen, Switzerland) to assess internal structure, pore size, and porosity. The device was pre-loaded with settings designed for bone and porous bone-like materials. The resolution for the scan was 37μm. Three 2x1x1cm 70% porous gyroid hydroxyapatite scaffolds designed for permeability testing and four 70% porous scaffolds of the morphology used in the clinical trial (matching the shape of the radius with a central canal) were scanned. Structures were manually contoured to fit their morphology so that no extraneous area was analyzed outside of the scaffolds. Values for total volume, material volume, mean spacing between struts, and mean strut thickness were returned by the device. Porosity was calculated using values for material volume (BV) and total volume (TV) as seen in the following equation:

$$\varphi\% = 1 - \frac{BV}{TV} * 100\%$$

3.5.3. Bending of PCL Support Sleeve

Four-point bending of the PCL sleeves was performed using the MTS 370 load frame (MTS Systems Corporation, Eden Prairie, MN). Four (n=4) second-iteration sleeves of each of three sizes; 100mm, 125mm, and 150mm, were tested. To create parallel contact points perpendicular to the load cell, PCL "wedges" were designed in Fusion 360, printed, and added to the sleeves 40mm apart on the compression side and 90mm apart on the tension side of the bend. The surface of the sleeve was lightly melted using a lighter and the wedges were adhered to the molten PCL. A custom four-point bending apparatus was attached to the load cell and the contact points were adjusted to meet the wedges. Sleeves were loaded into the device as seen in Figure 8 and bent at a constant rate until a 100N force was recorded. The slope of the bending curve in N/mm was recorded to determine stiffness. The total displacement at 100N was also recorded.

Figure 8: Design Iteration 2 loaded into the 4-point bending apparatus. 10cm, 12.5cm, and 15cm sleeves (right) were tested.

Because the length between contact points was held constant for each size, sleeve diameter and thickness are governing the change in stiffness rather than the length. However, these parameters were scaled 1:1 with the length, so the relationship between length and stiffness in this test is identical to the relationship between thickness and stiffness.

3.5.4. Mechanical Evaluation of Pre-Clinical Device

To evaluate stiffness in comparison to a traditional limb-sparing method, six canine cadaver limbs were selected from a pool of 12 cadavers at the surgeons discretion and complete device constructs (locking plate, PCL sleeve, scaffold) were installed using the standard surgical procedure (Section 3.6). Each leg was dissected so that the humerus could be potted and fit into a custom mount for an MTS 370 Load Frame equipped with an axial-torsional Load Transducer (MTS System). The limbs were loaded onto the mechanical tester with the paws at an approximately 60° from horizontal and the elbows extended to approximately 125° to best simulate the mechanical load experienced by the leg of a trotting dog[81]. An example of a mounted limb can be seen in Figure 9.
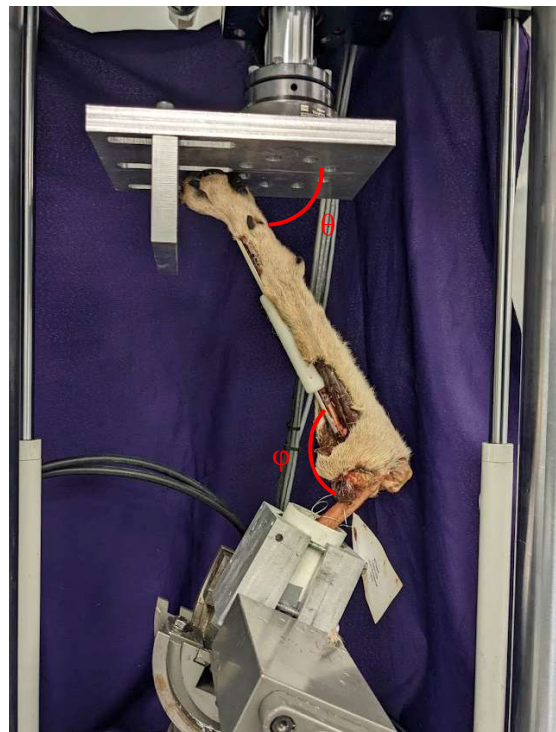
Figure 9: Canine cadaver limb #6 loaded onto the axial compressive testing apparatus. Θ was mounted to 60° and Φ was set to 125° to best simulate the load during the animal's natural gait

Each limb was compressed at a rate of 0.5mm/s following a sequence designed to minimize

hysteresis, in which the limb is first loaded to the static load of a standing dog and held for two

minutes. The limb was then loaded and unloaded to and from its walking load seven times,

followed by loading and unloading to trotting load three times. Specific loads calculated based

on the dog's original weight can be seen in Table 2. Static preload was calculated under the

assumption that the forelimbs carry around 60% of the dog's weight, which also corresponds to

peak vertical walking force of 6.35N/kg[82,83]. This amount doubles to 12.7 N/kg when the dog is

trotting at 2.84m/s[84].

Table 2: Mechanical loading of each limb. Calculated based on the weight (kg) of each
cadaver. Column 1 numbers correspond to the original cadaver's numbering.

Cadaver ID #	Limb (R/L)	Mass (kg)	Preload (N)	Walking Load (N)	Trotting Load (N)
2	R	18.2	53.56	115.57	231.14
4	R	22.8	67.1	144.78	289.56
5	L	21.4	62.98	135.89	271.78
6	L	25	73.58	158.75	317.5
8	L	19.6	57.68	124.46	248.92
10	R	19.4	57.09	123.19	246.38

Following testing of the full construct, the sleeves and scaffolds were removed using a rotary

saw. The same limbs were then re-tested with only the steel fixation plate installed. Finally, the

resected radii of the limbs were installed into the gap and fixed to the plate with two locking

screws each to simulate allograft installation and the limbs were each tested a final time. This

resulted in each limb having been tested in three conformations: Full construct, plate-only, and

allograft. It was ensured that each construct did not experience a force exceeding the yield

strength of the steel fixation plate so that the plates could be re-used in each construct without any permanent deformation. The ultimate walking and trotting curves were isolated and fit to linear trendlines, of which slopes were recorded to determine the full construct stiffness using a prior method[85].

3.6. Pilot Limb-Sparing Surgery and Clinical Trial

Prior to the opening of clinical trials, devices were installed in canine cadavers to allow the clinical oncologist to develop and optimize an installation process and to inform design changes to the device to ease the process, become more comfortable for the patient, and maximize clinical outcomes. Preparation and delivery of parts for cadaver surgeries also allowed the design/production team to assess the timeframe needed to prepare for these surgeries. It was decided that the timeline to create a full device after the patient's CT scan was 4 days. This gave the team the time needed to process the DICOM data, prepare HAp slurry, and design and print each component, as outlined in the workflow in Appendix E. A period much longer than this would have also required pre-surgical administration of anti-cancer drug therapy, which we wanted to avoid.

3.6.1. Selection Criteria and Initial Examination

The clinical trial was opened for recruitment of qualified prospective patients in October 2021 based on the following criteria: Canines must have malignant non-metastatic osteosarcoma with tumor growth occurring at the distal end of the radius. The distal radius was chosen since it has a lower risk of metastasis compared to other tumor locations and is ideal for limb sparing procedures, because arthrodesis of the radiocarpal joint is generally well tolerated[4,6]. Patients were to be no more than 85kg, no less than 20kg, and deemed healthy enough for surgery by their veterinarian. Three patients (Table 3) were chosen and underwent the procedure between

December 2021 and January 2022. A fourth patient underwent the procedure in May 2022 and will be further discussed in the Discussion section.

Table 3: Patient Information

Patient #	1	2	3	4
Breed	Great Dane	Great Pyranees/ Anatolian Shepard	Labrador Retriever	Malamute
Age (Y)	6.5	6.5	12.5	6
Weight (kg)	55	47	38	69
Sex	M	M	M	M
Sleeve Design Iteration	2	3	3	4
Plate Size (width, mm)	16	16	11.5	16

3.6.2. Resection of Distal End Malignant Radius

Patients were anesthetized with under the discretion of a veterinary anesthesiologist. For each procedure, a surgical incision was made on the cranial aspect of the afflicted limb, stretching from the metacarpals to the proximal end of the radius. The surgeon then prepared the area so that the cutting guide could be fit into place, contacting the proximal radius, the styloid process of the ulna, and the second and fourth metacarpals. The cutting guide was fixed to the radius and the two metacarpals with k-wire to ensure no movement occurred during the cuts. An oscillating surgical saw was used to perform one cut to the radius and one cut to the radial and ulnar carpal bones, 5mm below the antebrachiocarpal joint, allowing the tumor to be removed. After the ostectomy, the specimen was sent for radiograph imaging and histopathology. The surgeon also removed the periosteum from the portion of the radius that is inserted into the device, as is standard practice with this type of procedure.

3.6.3. Application of Bioceramic Endoprosthesis

Assembly of the device occurred predominantly prior to its installation. After sterilization, parts were sent to the operating room where they were assembled by a technician wearing a sterile gown and gloves. First, four ¼" x ¼" x 2" were cut from one ¼" x 1" x 2" sponge, included with the Infuse Bone Graft Kit (Medtronic). The sponges were loaded into the central canal of the TE scaffold. This involved tying the sponges to suture thread and pulling them through the scaffold, repeating for the necessary number of sponges to fill the length of the canals in each piece of scaffold. Next, the sponges were loaded with 1.4mL (2mg) of rhBMP-2 in a 1.43mg/mL solution, prepared according to the Infuse Bone Grafting Kit preparation guide. This was performed using two 1mL syringes by inserting the needles into the central canal and drawing the needle out while ejecting the growth factor. Scaffold pieces were then inserted into the PCL sleeve in order, beginning with the piece closest to the proximal end (the end contacting the radius).

3.6.4. Securing of PCL Support Sleeve and Surgical Plate

Prior to fixation of the surgical plate, the fit and alignment of the entire construct were examined by the physician by sliding the empty sleeve over the plate and placing it in the defect. They then determined the ideal angle at which to fix the radiocarpal joint. This angle varies by patient but is typically around 10 degrees. The sleeve was then removed to have the scaffold installed and a benchtop bending vice was used to bend the plates in the cranial direction. Five to six (depending on the patient) self-boring, locking screws were used to affix a steel fixation plate of either 11.5 or 16mm in width (Table 3; Veterinary Orthopedic Implants, St. Augustine, FL), to the radius

prior to fixation of the sleeve/scaffold complex. Bicortical screws were used in areas outside of the sleeve, while unicortical screws were used within the area of the radial/sleeve overlap. 3D printed PCL plugs were added to the screw holes that bridged across the scaffold to prevent any potential bone growth through the plate in the event future plate removal is desired. Once the fixation plate was secured, the surgeon was handed the sleeve, with the scaffold and growth factor already inserted, and the sleeve was slid around the plate and radius, with the sleeve overlapping the bone the length of 20% of the original length of the resected radius. Finally, the distal end of the fixation plate was screwed to the 3rd metacarpal using 7 bicortical, self-boring, locking surgical screws. Two screws were then drilled through the proximal end of the sleeve, affixing it to a single layer of cortical bone in the radius. Prior to closing, collagen sponges were loaded with appropriate doses of amikacin corresponding to 25mg/kg of the animal's mass and applied in the area surrounding the PCL sleeve. After closing, the patient received Nocita, a liposome-encapsulated bupivacaine, at a dose of 5.3 mg/kg to control pain. They also received fentanyl immediately post-op as a constant rate infusion of 2-5 mcg/kg.

3.6.5. Post-Surgical Clinical Schedule

The patients were allowed to return home after three days of monitoring in the hospital if they were eating and comfortable. A supporting bandage was placed on the patient for at least two weeks following surgery. Patients received oral painkillers in the form of Gabapentin 10-15mg/kg every 8-12 hours and Carprofen 2.2 mg/kg every 12 hours. Patients returned for recheck at the time of chemotherapy in the form of intravenous carboplatin starting 2 weeks after surgery and every 3 weeks for a total of 6 treatments spanning 18 weeks. Rechecks of the prosthesis were performed every 8 weeks. At the rechecks, the device is checked for complications via physical exam and radiographic analysis. Radiographs were also examined to

assess osteointegration and healing. Limb function was assessed at each recheck via a lameness exam (graded 0 to 4) and by measuring ground reaction forces using the pressure sensitive walkway (PSW). Between first and second recheck, certain patients were scheduled for a CT scan to help analyze osteogenesis within the scaffold.

3.7. Post-Surgical Analysis

3.7.1. Standardized Lameness Exam

Objective lameness exams were performed at each recheck and were graded according to the following scale:

Score 0 =Normal

Score 1 =Slight lameness (inconsistent lameness/lameness is difficult to observe or it is difficult to determine the affected limb)

Score 2 =Moderate lameness (clearly detectable lameness associated with <u>minor</u> head movement/pelvic tilt/forward or backward shifting of weight distribution [for bilateral lameness])

Score 3 =Severe lameness (clearly detectable lameness associated with <u>obvious</u> head movement/pelvic tilt/forward or backward shifting of weight distribution [for bilateral lameness])

Score 4 =Non-weight bearing lameness (regularly skips a few steps)

3.7.2. Pressureometry

Ground force reaction was measured using a pressure sensitive walkway (HRV Walkway 6 VersaTek System, Tekscan, Inc., South Boston, Massachusetts). Briefly, all dogs were acclimated to the gait analysis laboratory prior to their first trial until they showed no signs of anxiety. For the dogs able to ambulate without overt discomfort, six trials (three in each

direction) were acquired with a subjectively constant velocity, in a straight line, without lateralization of the head, pulling on the lead or stepping off the PSW. When dogs only tolerated to be walked in one direction, all trials were acquired in that single direction. Similarly, if the dogs only tolerated one or two trials over the PSW, no further trials were attempted to prevent exacerbation of pain. The dogs were walked over the PSW at their own comfortable speed within a velocity range of 0.8 to 1.4 m/s preoperatively. Trials from the subsequent visits for an individual dog were only considered valid if they fell within a velocity range of 0.3 m/s of their velocity established preoperatively. The labelling of each foot placement by the program was visually confirmed via review of the video recorded during the gait analysis data acquisition. The following parameters were calculated and averaged from the available valid trials of each visit for each limb: peak vertical force in Newtons and expressed as a percentage of body weight in Newtons (PVF%), vertical impulse (VI) in Newtons per second.

4. Results

4.1. Design Evolution

Throughout this project the sleeve underwent an iterative process that drove design changes. This cyclical process can be seen in Figure 10. It consists of four major steps during which a new design is developed, the design is tested to make sure it works for additive manufacturing, the design is delivered to the clinician who performs a cadaver or clinical surgery, and the clinician delivers feedback based on their impression of the device and or the surgical outcome. Finally, a new design is developed based on this feedback.
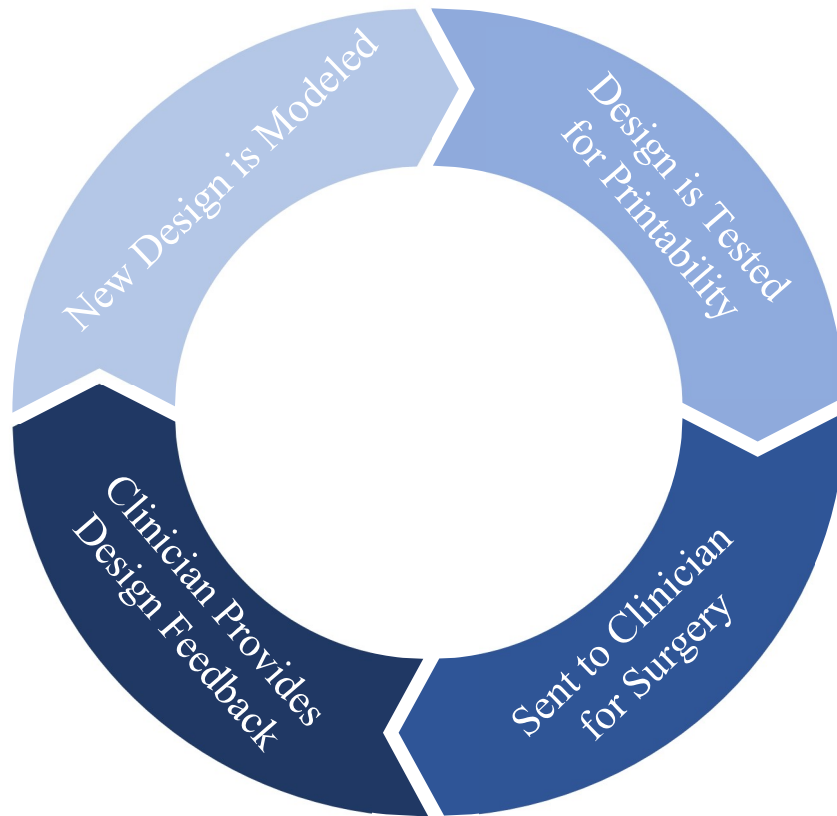
Figure 10: Iterative design cycle between the design/engineering team and the clinician

Four major design iterations occurred during this project, three of which were installed in the four clinical trial patients to date. Design changes between Iterations 1 and 2 occurred during

surgical protocol development and cadaver surgeries, while design changes between iterations 2, 3 and 4 all occurred during clinical trial. Each iteration's experiments and, if applicable, clinical trial surgeries will be discussed in detail.

4.1.1. Design Iteration 1

The first iteration of the sleeve (Figure 11) was cylindrical, with ribs running lengthwise for added structural support. The sleeve was surrounded by four cuffs meant to be slid over the plate and sleeve and screwed into the plate to share and transfer load and protect the scaffold. Small pores were placed between the ribs to enable transcortical flow.
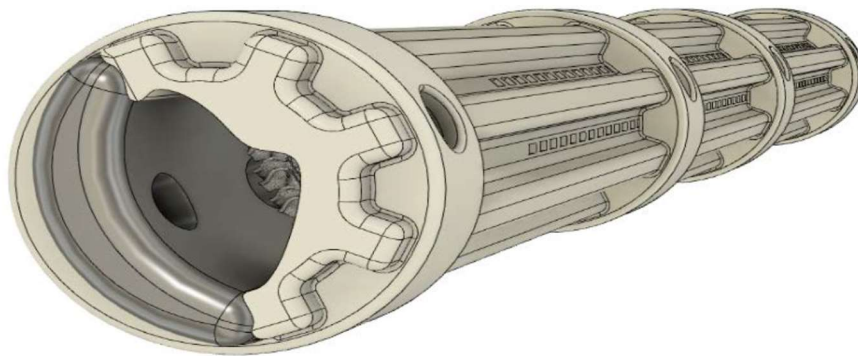
Figure 11: First iteration sleeve design with rib/cuff design

This design had several flaws that became apparent both during printing and during practice surgeries. First, this design did little to limit the complexity of the surgical process, as the four rings needed to be added in a specific order and individually screwed to the plate. From a 3D printing perspective, the rings also needed to be much thicker than designed so the thinnest part of the ring (the parts sliding over the ribs) was not so thin as to become a failure point. The thickening of the rings caused concerns that the sleeve could lead to stress concentrations on the wound closure, increasing chances of infection and improper healing. Finally, the plate

interaction with the scaffold was cause for concern on two fronts. It was determined that the scaffold was far to brittle to accommodate the plate screws, so these screws were removed from the design. There was also concern that the direct contact between the steel plate and the brittle scaffold could lead to scaffold failure under load-bearing conditions.

4.1.2. Design Iteration 2

A new design was developed in response to the analysis of the first iteration. This new design (Figure 12) simplified the surgical process by consolidating the ring/sleeve complex into one piece that could easily be installed in a single step by sliding the sleeve over the plate from the distal end. The single component design slightly reduced thickness because the design thickness is controlled by keeping the thinnest part of the sleeve at minimum 2mm. A rail of PCL was also added within the sleeve to separate the plate from the scaffold. The pores were retained and remained small. This design was implemented during the pilot surgery on Dog #1 and was the subject of the 4-point bending study.
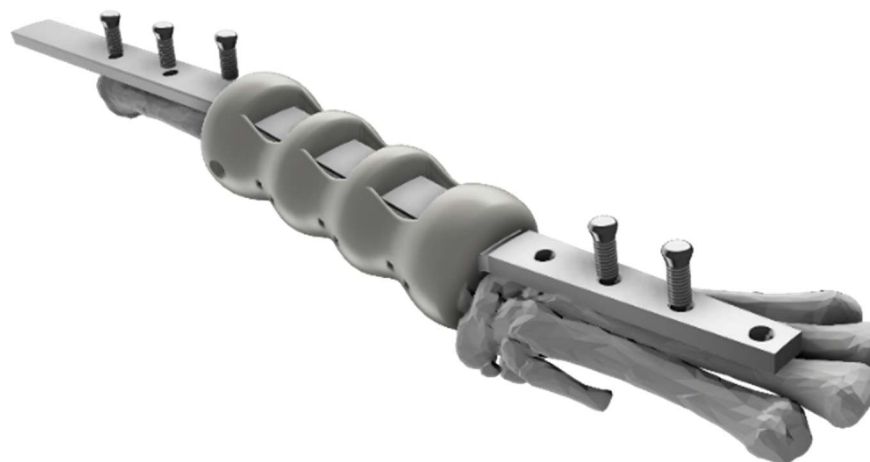
Figure 12: Second design iteration with incorporated cuffs

Although this design was thinner than the first iteration, the closure of skin around the thicker "ring" areas remained tight, and there was concern that this could cause discomfort to the patient.

The "windows" between the rings were also deemed to be unnecessary and were removed in later iterations. Another major concern that arose during installation was that the device had much more contact with the accessory carpal bone than expected, and it became clear that patient-specific design was needed to create space for this bone.

4.1.3. Design Iteration 3

To further thin the sleeve and drastically simplify the design, a cylindrical design was returned to, with no windows over the plate. These windows were originally designed for the placement of collagen sponges holding antibiotic, but the surgeon decided instead to apply antibiotic to the entire surrounding area, making the windows unneccessary. Though the thickness was determined in the same way, the more uniform thickness was less likely to result in stress concentrations in the surrounding skin tissue. This iteration was implemented during clinical trial surgeries on Dogs #2 and #3, and was the model installed in cadaveric limbs for mechanical testing.

Figure 13: Third iteration and primary subject of this study

This design was successful in protecting brittle scaffolds under anatomical load in both cadaveric testing and clinical trial, but concerns remained about the thickness of the device.

4.1.4. Design Iteration 4

This design was developed toward the end of the project's timeline, with the major goals of further reducing sleeve thickness and greatly opening up the sides of the sleeve to transcortical flow. This was accomplished by, instead of a cylindrical design with a Boolean difference, taking the shape of the radius and offsetting by only 1.6mm. This design was implemented in clinical trial in Dog #4.

Figure 14: Fourth design iteration with dramatically reduced thickness

It is believed that this sleeve will provide much less discomfort to patients because of its reduced thickness. Despite the much sleeker design, results from the mechanical testing of cadaver limbs (described below) suggest that this sleeve will still provide sufficient support to the scaffold.

4.2. Device Characterization

4.2.1. Permeability

The manometer method of calibration provided a very accurate standard curve (Figure 15) with which it was possible to translate voltages into pressure values. The R^2 value is 0.99, indicating a very accurate linear fit. The equation of the linear fit line was therefore used to calculate pressure differentials from experimental data.
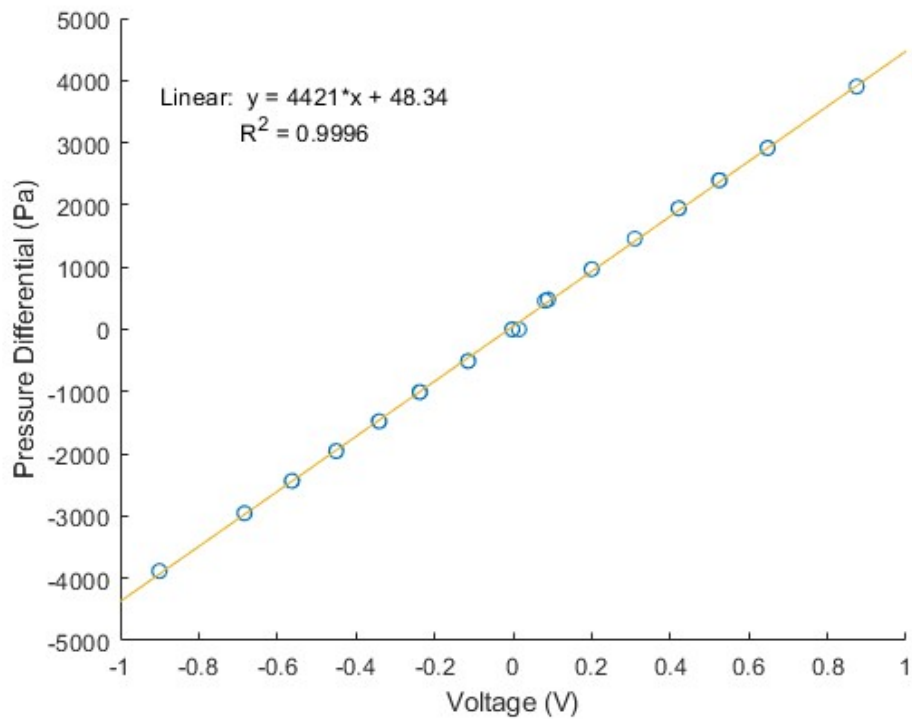
Figure 15: Standard curve relating the voltage output from the pressure transducer to pressure differential across the device.

It was discovered that the pressure differentials returned at 10mL/min and 20mL/min flow rates were beneath the P55 transducer's range, and these values are therefore not reported. Average permeabilities for the other three flow rates (30, 40, and 50mL/min) are reported in

Figure 16. Permeability values for the longer (3cm) scaffolds tended to be slightly higher but with more variation, while the 2cm scaffolds were more consistent. Due to the larger variation of the 3cm scaffolds, no significant trend can be declared, but the values can still be used as means for comparison with the permeability of trabecular bone. All mean values fell between 1100 and 1400μm^2.
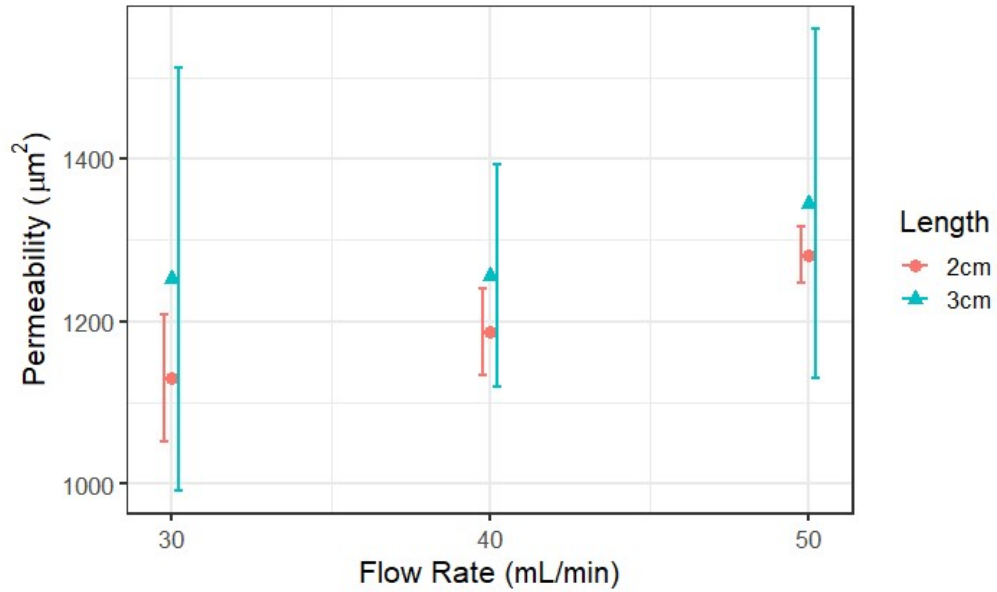
Figure 16: Darcian permeability values for n=6 scaffolds at each length and flow rate with standard error bars.

4.2.2. Bending Stiffness of Sleeves

Figure 17 shows the bending stiffnesses determined by the four-point bending of sleeve iteration 2. Unsurprisingly, a trend shows the stiffness increasing as radius and thickness do, with the 12.5 and 15cm groups being significantly stiffer than the 10cm group.
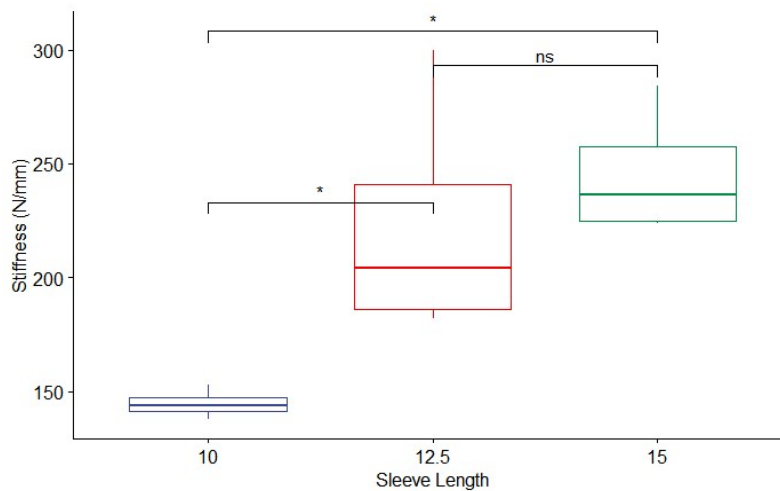
Figure 17: Boxplot of stiffness values for the 3 sleeve lengths tested

It should be noted that, while not statistically an outlier (Grubb's test p-value=0.10), the highest value for the 12.5cm sleeves was unusually high at 299N/mm. If this value is removed from analysis, all three groups were statistically different from one another.

4.2.3. Porosity, Pore size, and Strut Thickness

The results of μCT scans of hydroxyapatite scaffolds are summarized in Table 4.

Table 4: Summary of μCT porosity (φ) results. Columns 1 and 2 correspond to the two morphologies of scaffolds scanned. Column 3 contains mean values for all seven samples.

Sample Morphology	Cubic (n=3)	Clinical (n=4)	All (n=7)
Mean φ (%)	63.91	66.3	65.3
Standard Error	0.57	0.66	0.64
$\Delta\varphi$ (%)	6.09	3.66	4.70
Mean Spacing (mm)	0.722	0.724	0.723
Mean Thickness (mm)	0.427	0.421	0.424

Mean porosity (φ) was found to be roughly 5% lower than the designed porosity of 70%. This is due to an inaccuracy in the printing process, in which extra material is deposited on the perimeter of the layer during non-printing moves, when the printhead is moving but is not meant to extrude material. This occurs due to the oozing of extra material while the printhead is not actively extruding, caused by backpressure in the print head. Figure 18 shows a thickness map of two μCT-scanned scaffolds. These depositions of extra material can be seen in the red and orange-colored areas corresponding to thicker portions of material at the perimeter of the layers.
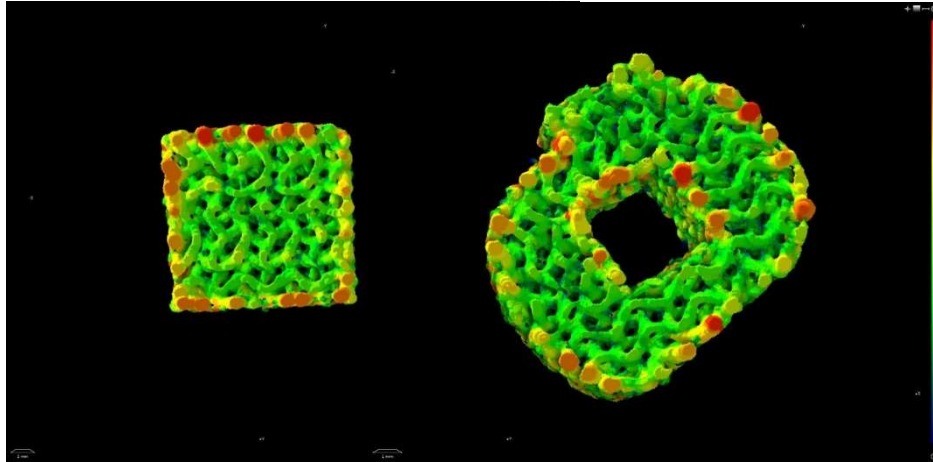
Figure 18: Thickness map of cross sections of two μCT scans of gyroid scaffolds. Left: cubic morphology. Right: Clinical morphology. Colder colors correspond to thinner sections of material, warmer sections correspond to thicker sections.

The mean spacing (723 ± 5μm) and strut thickness (424 ± 4μm) were quite consistent between scaffolds and were as-expected for similar scaffolds of this type in literature. Consistent strut width verifies our printing method's repeatability in that it is shown to produce near-identical scaffold structure between prints. Manual measurements were taken of the space between struts using the CT images This was done to verify that the mean spacing reported by the software program was accurate. Figure 19 demonstrates how these measurements varied in width within each scaffold, while illustrating measurements listed in Table 4. The strut thickness as measured was consistent with the size of the 22-gauge nozzle used to print. The program did not give a definitive value for pore size which, in gyroids, varies along the interconnected pore and is similar to the spacing value, as seen in Figure 19. It is defined as the diameter of the circle inscribed between struts of a unit cell in planer view[86], which varies from approximately 585μm to 703μm.
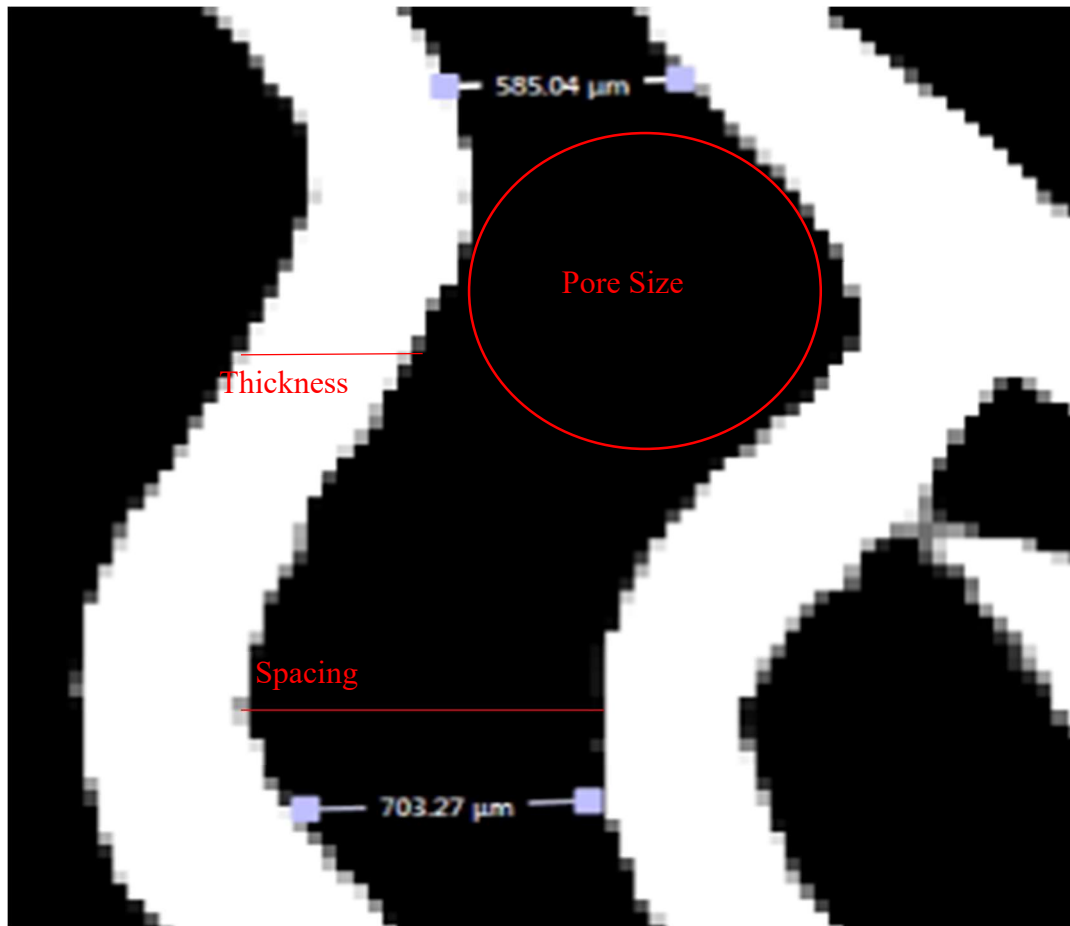
Figure 19: Measurements for the spacing between roads using the µCT visualization software.

4.2.4. Axial Compression of Cadaver Limbs

Individual cadaver limb stiffnesses (N/mm) for each limb in each configuration can be seen in Figure 20 at both walking and trotting loads. Because the limbs were loaded at an anatomical angle, stiffness values were lower than those of similar studies in which the limbs were loaded perpendicular to the load cell[85,87].
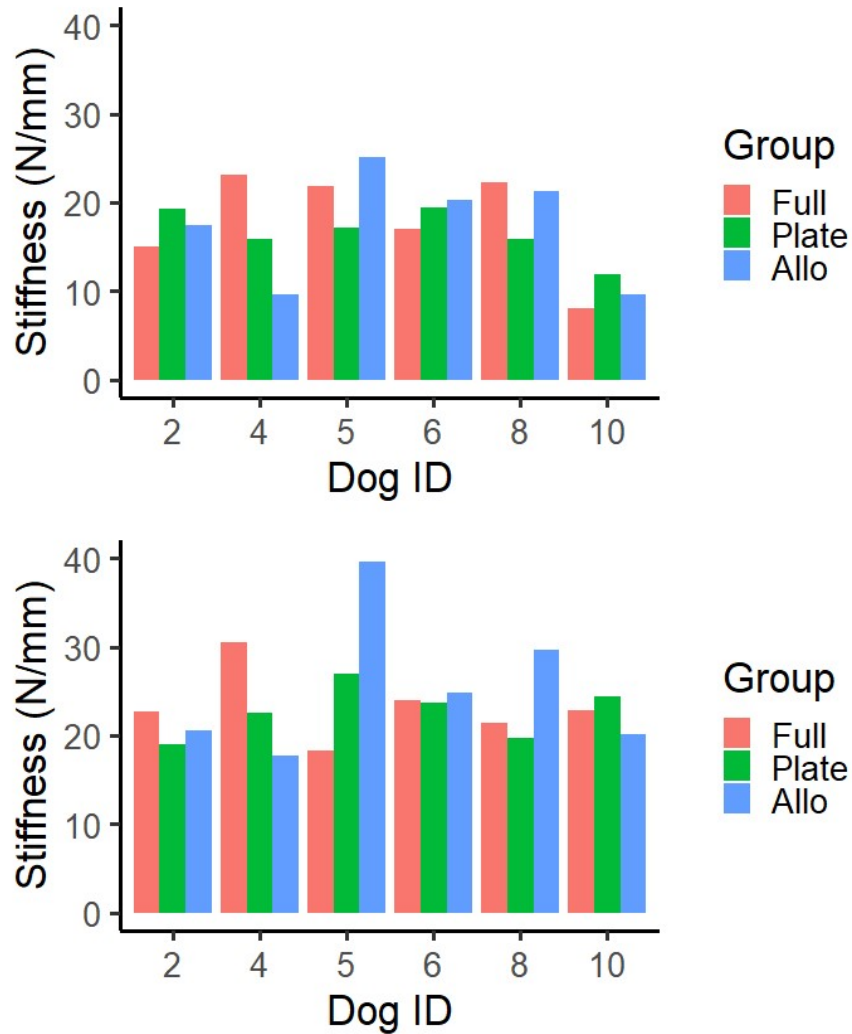
Figure 20: Full-construct stiffness of each construct at A) walking load and B) trotting load.

While Figure 20 shows some variation between individual tests, stiffnesses were overall very consistent across the six limbs and three constructs. This can best be seen in Figure 21, which shows that for both walking and trotting loads, no significant differences exist in stiffness between the three constructs. ANOVA analysis of the three groups revealed very low likelihood that any differences exist between any two of the three groups at both walking and trotting loads ($p = 0.91$ and $p = 0.64$, respectively).
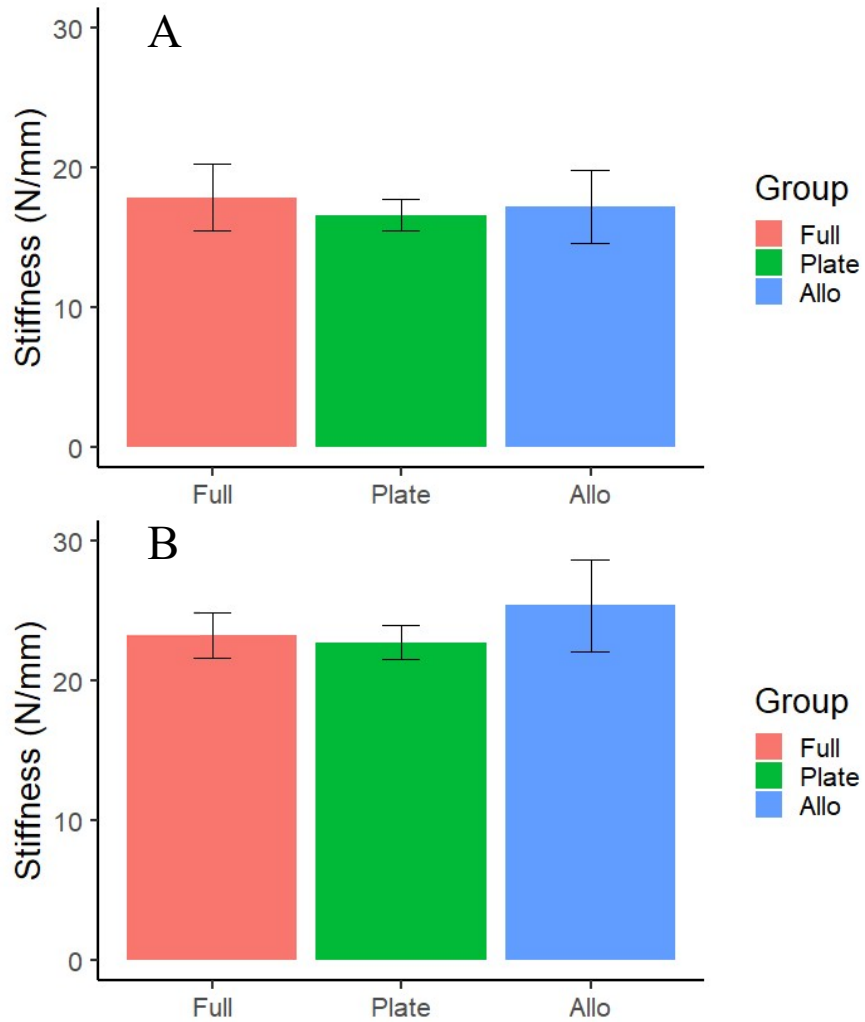
Figure 21: Average (n=6) full construct strength of each construct at A) walking and B) trotting loads.

Little damage was inflicted on the osteogenic TE scaffolds during testing. Figure 22 shows one of the sleeves removed from the cadaver limbs with the scaffold still intact, which was consistent across all tested scaffolds. All four pieces of scaffold remained in good contact with one another, indicating that the sleeve performed well to immobilize the scaffolds.
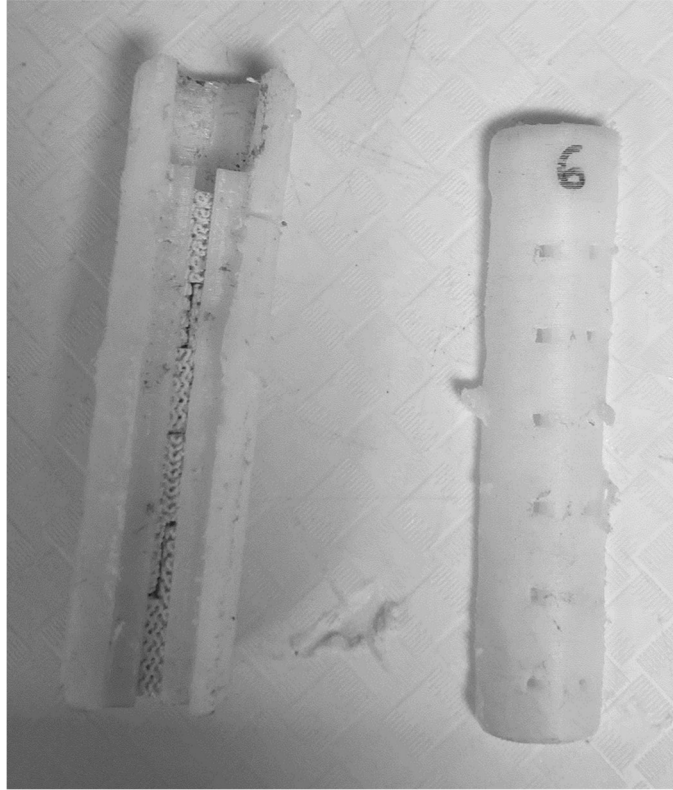
Figure 22: Image showing the intact scaffold within the sleeve after it was removed from the cadaver limb/plate construct.

These results are planned to be used as a basis for comparison with limb testing performed after the patients perish. It is expected that the device will be somewhat incorporated with the limb via the formation of natural bone, so the limbs tested at the end of the study will only contain the full construct group.

4.3. Clinical Trial

Four devices were successfully installed in pilot clinical trial surgeries. Three of the patients can be seen in Figure 23.

Figure 23: Clinical trial patients. Left: Dog #1 (Groot) post-op. Center: Dog #3 (Mad Max) post-op. Right: Dog #4 (Onyx) pre-op.

Unfortunately, the operated limb of one of the patients needed to be amputated for reasons unrelated to the device, leaving three animals with the device installed during their recovery.

4.3.1. Dog #1

The pilot surgery of this project occurred on November 30, 2021. The patient was a 55kg Great Dane named Groot. Groot qualified for the trial with non-metastatic osteosarcoma of the right distal radius and had the full second iteration device installed in the 13cm defect caused by his ostectomy. During the procedure it was noticed that the channel in the sleeve for the plate to fit through was much too tight. Previous designs with similar tolerance had resulted in ideal fit for the plate, but this specific sleeve was not checked for plate fitment prior to delivery. Subsequently, all sleeves were checked for plate and scaffold fitment prior to delivery to the clinic. As a result of this complication, a soft mallet was used to tap the sleeve onto the plate and proximal radius, which resulted in fracture of the distal end of the scaffold. The second complication during this surgery was that the caudal aspect of the sleeve was impacting the

51

accessory carpal during attempted installation. Because the accessory carpal is not essential for limb function after limb-sparing surgery, the decision was made to remove the bone so that the sleeve could safely be installed. The fully installed device was radiographed immediately post-operatively, and at each 8 week follow-up. These radiographs can be seen in Figure 24. The sleeve is not visible as pure PCL is radiolucent.
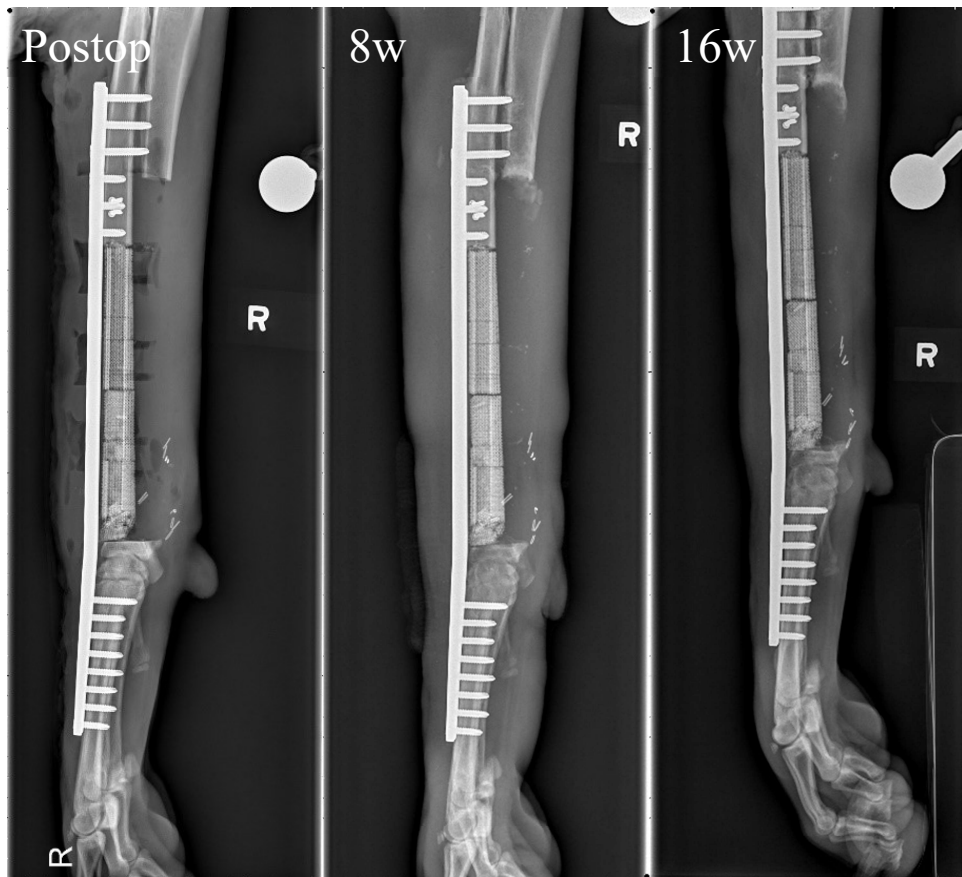
Figure 24: Dog #1 (Groot) lateral radiographs taken at post-op, 8 weeks and 16 weeks.
The radiographs show that despite the shattering of the distal end, the scaffold has remained completely intact thus far. Even the portion that experienced heavy fracturing appears to have remained immobilized in the distal end of the sleeve. As of the last set of imaging, no observable bone growth, which would show "cloudiness" or smoother portions of the scaffold similar to the bone, is present.

Limb sparing surgeries are associated with quite poor limb function for a period of time following the procedure. Unsurprisingly, objective gait analysis and pressureometry both indicated quite poor limb function initially. However, weight distribution in the forelimbs has shown a return to normal after about 4 months (Figure 25).
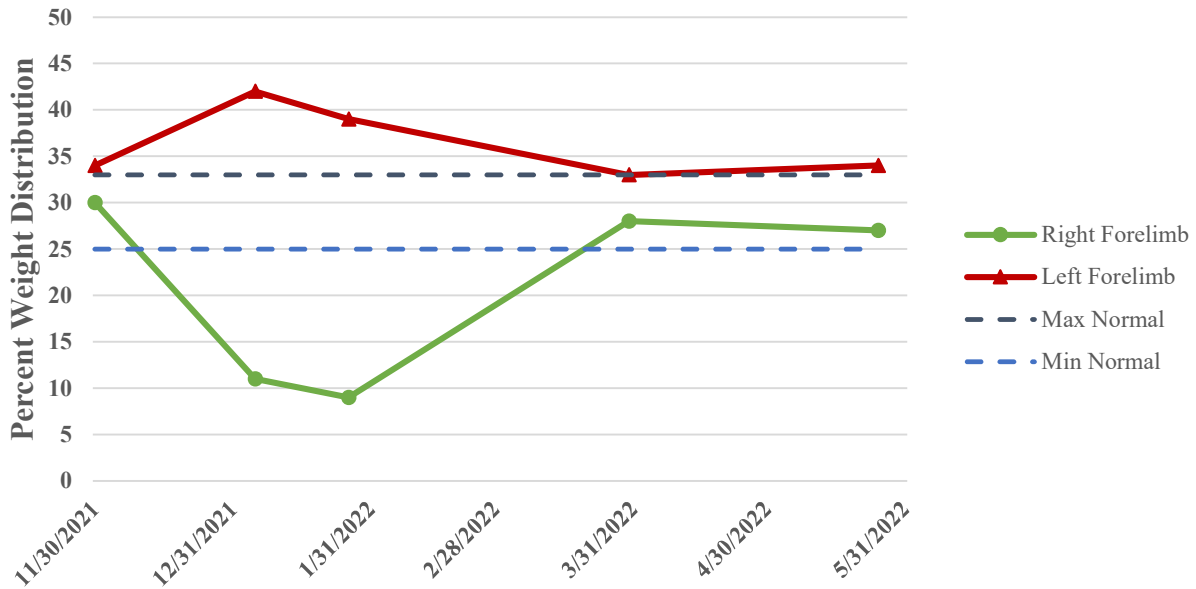
Figure 25: Percent body weight distribution by limb. Values for 11/30 were taken prior to surgery.

Canines typically carry around 60% of their weight split between their forelimbs, with each limb carrying between 25-33%[88]. Groot was observed to have mostly normal distribution prior to his surgery, slightly favoring the non-diseased limb, but heavily favored the unoperated limb afterward with the left limb carrying as much as 42% of the weight and right limb carrying as little as 9%. As of his 16 and 24 week rechecks, however, weight distribution has returned near to pre-surgical values for both legs and appear to have steadied out. This is reflected in the lameness scores seen in Figure 26.
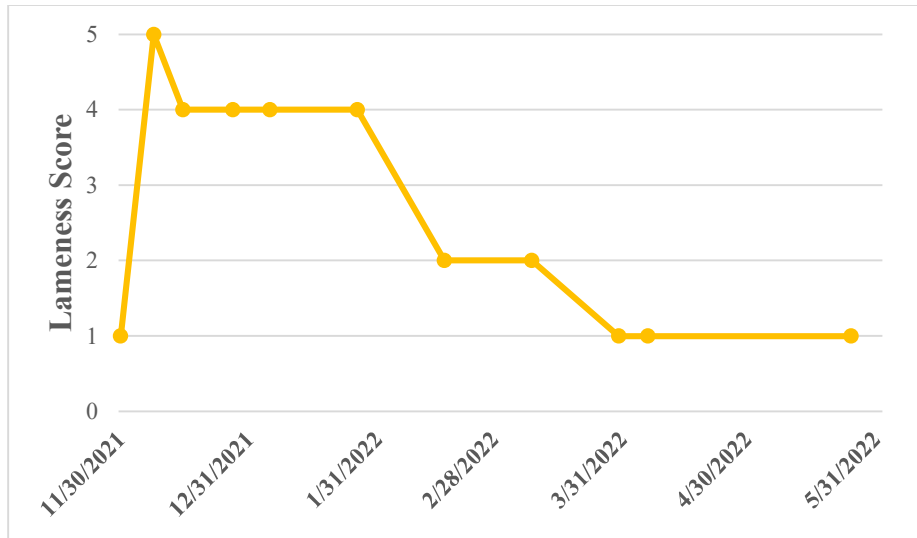
Figure 26: Lameness scores for Dog #1 (Groot)

This patient also had a CT performed when it was noticed that no bone growth was noticeable at 8 weeks. The CT was performed at approximately 14 weeks. Despite some aura from the steel plate interfering with the imaging, the lattice of the gyroid scaffold was still visible (Figure 27). Once again, no clear indications of osteogenesis were observed.
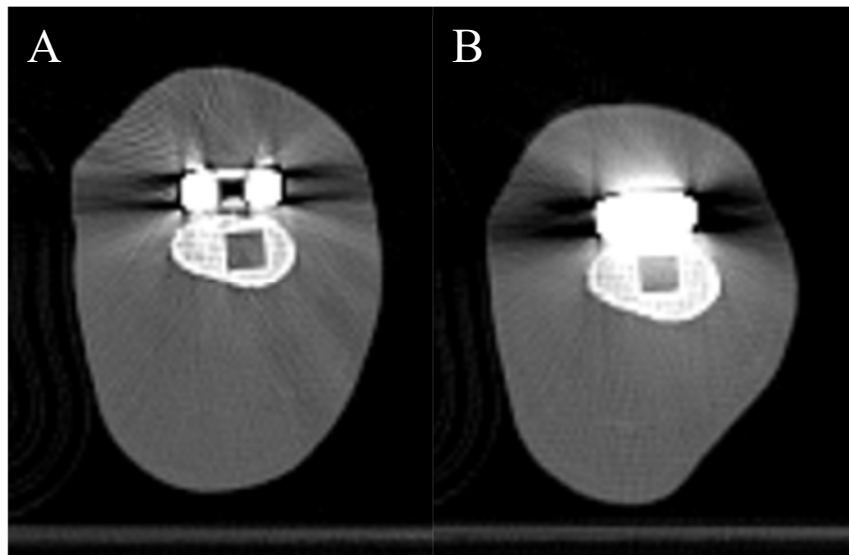
Figure 27: CT layers of Dog#1 showing cross-sections of the scaffold at the A) proximal end and B) midway down its length.

4.3.2. Dog #2

The second surgery took place on January 18, 2022. The patient was a 6.5-year-old great Pyranees/Anatolian Shepard mix named Lefty who weighed 47kg. Lefty presented with a large osteosarcoma of the right distal radius. Between the time when the CT was taken and the surgery was performed the tumor had also grown faster than expected. This caused several complications to arise. First, the cutting guide, specifically the "arm" of the guide that wraps around the distal head of the ulna, was unable to fit as designed. The tumor had also grown to a size that necessitated removal of the carpal bones. Therefore, the cutting guide was cut at the arm and only the proximal half was used, with the removal of the bones acting as the distal cut. Despite this, the scaffold and third iteration sleeve were successfully installed. Pre and postoperative radiographs can be seen in Figure 28.
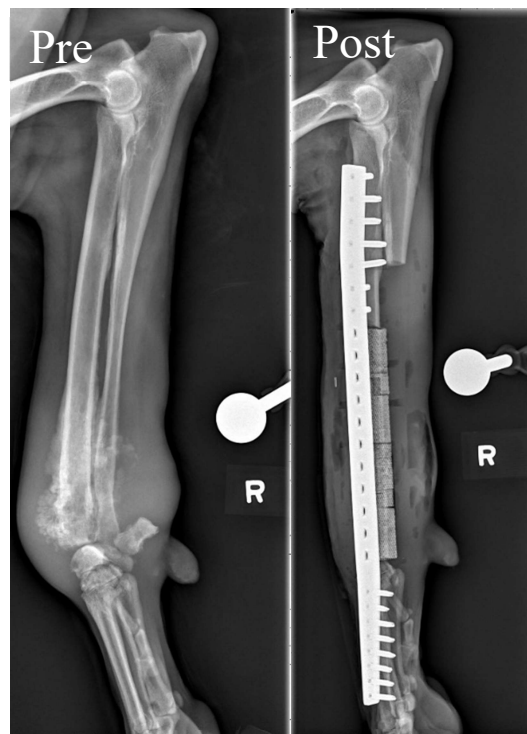
Figure 28: Pre and postoperative lateral radiographs of Dog #2 (Lefty)

Unfortunately, the skin surrounding the tumor site experienced necrosis shortly after the surgery. The size of the tumor had put excess stress on the area, and the amount of soft tissue required to be removed because of the spread of the tumor had compromised blood flow to the area. So, despite successful installation of the device, the limb was amputated less than a week after installation and, consequentially, no long-term data was acquired.

4.3.3. Dog #3

The third clinical trial surgery was performed on January 21, 2022, on a 12-year-old Labrador retriever named Mad Max. Due to the quick turnaround between the second and third surgery, no design changes were made between them. Therefore, Mad Max also received the third iteration of the sleeve. This procedure did not experience complications and the device was successfully installed. After 4 weeks, the patients owner became concerned that limb function was not improved and had the primary veterinarian take a radiograph of the device (Figure 29). It was at this time that what appeared to be mineralization surrounding the PCL sleeve was observed. The same phenomenon was observed at his regular 8 week recheck but appeared to have remained static and not continued to develop. The mineralization was aspirated, and results indicated that it was not local cancer recurrence.
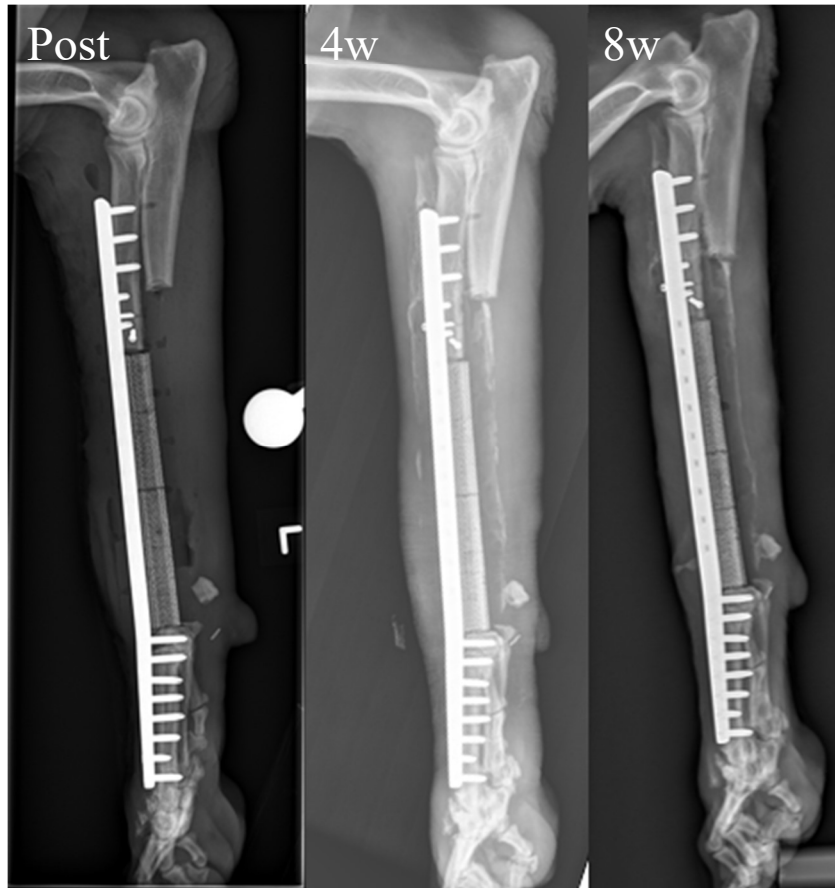
Figure 29: Post-operative, 4 week, and 8 week lateral radiographs of Dog #3 (Mad Max).

This patient experienced a variety of complications during his recovery. Primarily, a failure of

the wound closure due to the patient scratching at the device made healing very difficult, and led

to infection, which was treated with multiple rounds of antibiotics. This inhibited the patient's

ability to return to a normal gait, though it should be noted that this animal was quite elderly and

arthritic and was heavily favoring his right limb prior to surgery. The weight distribution to the

forelimbs at each recheck can be seen in Figure 30.
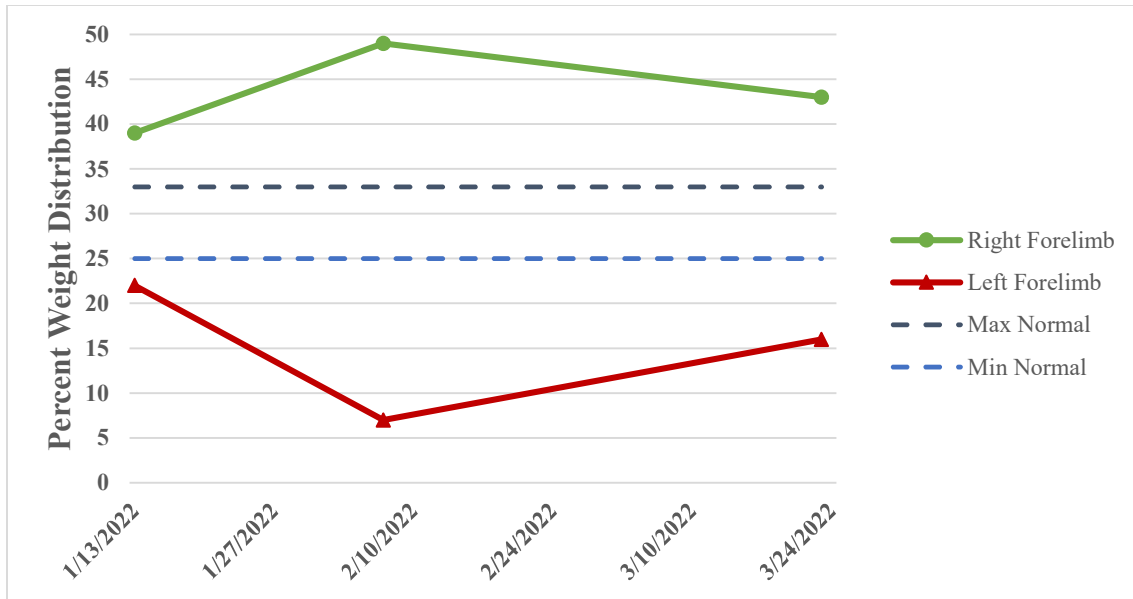
Figure 30: Percent of weight distribution to the forelimbs at each recheck for Dog #2. Values for 1/13 taken prior to procedure.

Though the operated limb still had a heavy limp, its percent of the weight bore increased from only 7% to 16% between first and second recheck. Lameness scores were in the range of 2-3 during this time. In late April 2022, the patient's owner reported a bleeding, protruding lesion on the animal's leg. On May 10, 2022, the patient was confirmed to have local recurrence in the limb via histopathology. The patient passed away on June 1, 2022, and the operated limb was returned to the Colorado State University Veterinary Teaching Hospital for analysis. During necropsy of the limb, it was discovered that the manus had healed to the scaffold, to the point at which the scaffold broke rather than separating from the manus. Histopathology results from the limb confirmed that the mineralization was not tumor growth, and was identified as mature bone and cartilage proliferation. The scaffold is planned to undergo μCT for further analysis of osteogenesis within the scaffold.

4.3.4. Dog #4

A fourth clinical trial surgery was performed on May 5, 2022, with several changes to the device. First, design Iteration 4 was used, which cut down on the space occupied by the sleeve and opened the sides of the device much more to enable more transcortical flow. Next, the scaffold material for this device was β-tricalcium phosphate (β-TCP), a ceramic similar to HAp that has shown faster bioreplacement and is also very commonly used with rhBMP in tissue engineering[21,23,89]. A method for photocasting using β-TCP had not previously been developed and the material was therefore not available for the first three patients of this trial. The patient for this procedure was a 69kg malamute named Onyx, with a tumor of the distal right radius. The patient had a fracture present in the tumor, causing concern that the antebrachiocarpal joint had been compromised by tumor cells. The radial, ulnar, and accessory carpal bones were therefore removed during this procedure. After removal of these bones, the defect would total 14cm in length. The device was successfully installed, which can be seen in the postop radiograph in Figure 31.
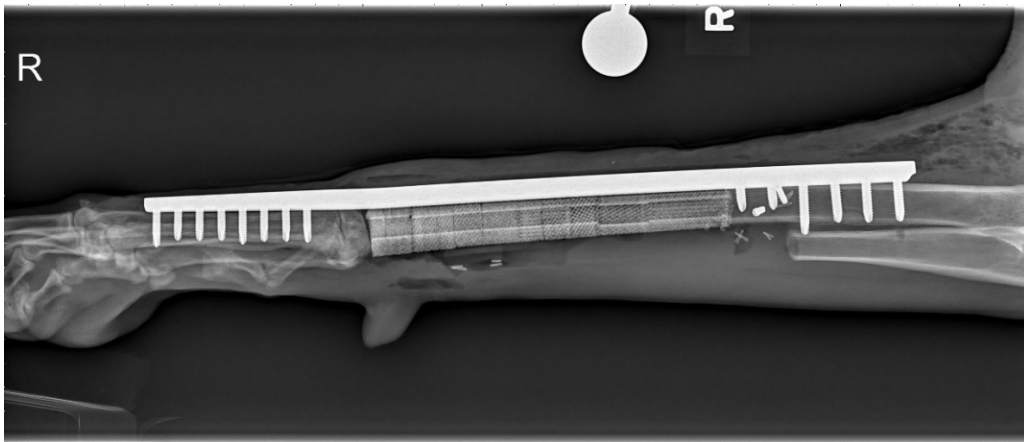
Figure 31: Postop radiograph of the full device installed in Dog #4 (Onyx).

Because this device was installed late in the project, no re-checks have been performed and therefore no follow-up data is available. However, the opening of transcortical flow coupled with

the osteogenic capability of β-TCP present exciting potential for this project. The thinner design

of the sleeve also made installation and closure of the wound much less complicated.

5. Discussion

5.1. Current Sleeve Design

Though the 2nd and 3rd iterations of the sleeve design were successfully installed, it was noticed by the clinician each time that the skin closure around the sleeve was quite tight, inflicting stress on the wound closure. Therefore, a recurring goal was to reduce the thickness of the sleeve, especially on the cranial aspect where the skin closes over the sleeve. Prior to mechanical testing of the full construct, it was unknown how much PCL material could be sacrificed to accomplish this thinner design and maintain sufficient strength. Once it was determined that the role of the sleeve was to fix and immobilize rather than contribute to the full construct stiffness, the fourth iteration of the sleeve was developed. This design is the current culmination of the iterative design cycle discussed previously. It is believed that these latest changes will further ease the installation process and improve patient comfort. Feedback from the clinician after the 4th surgery has confirmed that the stress on the wound closure is reduced and that installation was easier because of the reduced size.

Despite the constant drive for design improvements, all devices installed in clinical trial were successful. They were installed with minimal alterations to the standard limb-sparing surgical procedure. With the help of a device technician, the surgeon can simply slide the sleeve (already containing the scaffold with BMP) over the plate and continue with the normal plate installation. This means that it is not difficult for any physician capable of performing limb sparing-surgery to install the device, especially if there is a clear line of communication between the physician and design team. To that effect, through this process it became clear that certain engineering considerations were critical. The tolerances between the sleeve and the scaffold, plate, and radius

were essential for the ease of installation. If the sleeve fit too tight on any component it was very difficult to install, and the scaffold was at risk of breaking, which occurred at the distal end during the pilot surgery of Dog #1 due to hyper-compression. If any component was too loose the scaffold would be insufficiently immobilized or the precision of the fit would be compromised. Designing a sleeve with the perfect balance, accomplished through careful design and verification of fit prior to the delivery of parts, saved a great deal of installation time.

The success with which each device was installed is very promising for the future of this technology and indicates that one of the specific aims of this study, which was to develop a surgical procedure for the installation of the device, was a success.

5.2. Mechanical Behavior and Scaffold Support

The primary finding of the cadaver limb mechanical testing is that the presence of the sleeve-scaffold construct does not disturb or alter the stiffness of the full limb-salvage construct when compared to the gold-standard procedure (the allograft). While the sleeve and allograft provided stabilization as compared to the plate-only model, stiffnesses remained similar because the steel plate was the primary contributor to the stiffness of all three constructs, as expected. This is encouraging because, as this method proves useful in reducing scaffold failure, it can easily be incorporated into a standard limb sparing surgery without affecting its strength as a construct or disturbing the natural progression of the procedure. It also showed no negative effect on the functional outcomes of the limbs, with clinical trial patients regaining limb function similarly to gold-standard limb-sparing devices.

The sleeve's expected tendency to increase in stiffness corresponding to the thickness of the material was demonstrated via bending stiffness testing. However, the stiffness of the full construct did not scale with the mass of the dog (which corresponds to the thickness of the

sleeve). Though it was originally thought that increasing sleeve size to account for the mass of the dog would affect the stiffness of the construct, when the stiffnesses were normalized via their respective masses (Table 2), no effects on the results were observed, as there remained no difference in stiffnesses between constructs. This is likely because the plates are such a major contributor to construct stiffness and are available in only a few sizes. Therefore, there is no explicit need to scale the thickness of the PCL sleeve based on the size of the dog, other than to adapt its geometry to the larger size fixation plate, the use of which is determined by the surgeon. This means that the design of these devices can become much more standardized in the future, with two baseline designs (one for each plate size) that can be adapted to be patient specific by adjusting the proximal and distal ends of the sleeve to fit the host bone (from patient CT data). In the future, it will be advisable to test limbs containing the larger plate model to determine how stiffness compares, but only smaller plates were used for this test due to availability of cadavers and to accommodate the size of the mechanical testing device.

Importantly, scaffolds remained intact within the sleeves during testing at anatomical loads, as was observed after they were removed. This inspires confidence in the sleeve's ability to fulfill its primary design objective of keeping osteogenic but brittle scaffolds intact under the anatomical loads of the patients. This is further supported by the fact that no scaffold failure has been observed in the radiographs of clinical trial patients, who have been providing such loads repeatedly over the 3-6 months that the devices have been installed. It remains to be seen how the fourth iteration of the sleeve will compare mechanically, but because it was determined that the stiffness of the sleeve is not a governing factor, it is predicted to provide the same structural support and scaffold protection as its predecessors. There is evidence, in fact, that the thinner sleeve will be advantageous for the stimulation of bone growth because it will allow for micro-

motion of the scaffold. Wazen et al. (2013)[90] found that micro-motion based strain can influence early bone regeneration at the bone-implant interface. While motion above a certain threshold, which is restricted in our case by the sleeve/plate construct, can negatively affect ossification, micro motions show positive effects, increasing mineralization and decreasing the formation of unwanted cartilage[91].

It is expected that these results of this study will be viable for comparison to similar testing performed on additional clinical trial patients' limbs after they perish. Changes in stiffness during the trial could potentially occur via multiple mechanisms. First, if the device can grow bone sufficient for bridging, the scaffold stiffness would rise due to the osteotomy site being filled with natural bone. If union were achieved connection at the transition zone would increase the stiffness of the whole construct. Second, although the device is fixed at its proximal end over the radius with fixation screws, it is not fixed at the distal end in the epiphyseal model used in this study and therefore provides no resistance to the natural torsion that occurs during the patient's gait. Arthrodesis of the radiocarpal joint and union at the distal end of the scaffold could potentially create more resistance to torsion, altering the mechanism of the limb during testing. Many studies of this sort emphasize the need for strong fixation/immobilization of the scaffold, and the importance they have for achieving union. Morys et al. (2015)[92] found that stronger fixation resulted in a stronger construct with increased torsional stiffness. The strong fixation provided by the locking plate/sleeve construct will therefore encourage stronger union at the scaffold/bone interfaces, which has already been seen in Dog #2. Finally, it is important to remember that in other studies the final testing still may be influenced by remaining polymer additives in the scaffold. Because our device uses purely ceramic scaffolds, they will be replaced by solid bone sooner than a composite scaffold, and the final mechanical properties will be more

indicative of the healed bone. All these mechanisms are important to consider because, unlike some other studies, this study mimics the natural gait of the animal as closely as possible.

5.3. Permeability

Preliminary testing indicates that the scaffolds used in this project have ideal permeability for their application. Grimm and Williams (1997) found that trabecular bone ranges in permeability from $0.4\text{-}11\text{x}10^{-9}\text{m}^2$, corresponding strongly to porosities from 78-92% through a linear relationship[63]. The permeability of the 70% porous gyroid scaffolds used in this project was found to range from $1.1\text{-}1.4\text{x}10^{-9}\text{m}^2$. The scaffold was able to achieve similar permeability at a lower porosity thanks to its repeatable, interconnected gyroid structure compared to the more chaotic structure of the trabeculae. It is predicted that at flow rates lower than 30mL/min, a much lower pressure drop will be observed across the scaffolds, corresponding to higher permeability, but a differential pressure transducer that is more sensitive to lower pressures is needed to take these measurements.

The analytical model developed by Asbai-Ghoudan et al. (2021)[47] predicted permeability for several TPMS structures at various porosities using CFD, and modeled 70% porous gyroid permeability on the scale of 10^{-8} - 10^{-7}m^2 depending on pore diameter. However, they emphasized that while CFD typically matches empirical data in trend, the former is typically quite a bit higher, and a scaling factor is needed to account for things like real-world defects and surface interactions. It is difficult to compare permeability values between studies because of this. It can also be difficult to compare between empirical studies because of all the factors that have influence over permeability. One would need to find a study with identical morphology, porosity, pore size, material, production method, unit cell structure, and scaffold size. However, the fact that our values matched that of trabecular bone and are on the same scale as similar

scaffolds indicates that the scaffolds used for this study are capable of supporting the necessary flow needed for cell and nutrient delivery, and therefore osteogenesis.

Further study is needed to determine the precise permeability of the scaffolds in the shape used in device implementation. The measured permeability of the gyroid indicates that fluid will be able to permeate into the scaffold, but it is possible that the unique shape and open central canal are preventing flow to the outer perimeter. The scaffolds used in clinical trial are much longer than those tested, so a method for determining how fluid permeates through more complex shapes will be needed. The two lengths tested did not provide a clear trend, but it is likely that further testing with more precise equipment will. Flow into the scaffold will likely be aided by the opening of the sides of the sleeve in Iteration 4, as more flow in the transcortical direction will be possible.

"Ideal" pore size for bone tissue engineering scaffolds is typically reported to be 200-500μm. Pores that are too small require very thin strut length to remain above 50% porosity, and can experience pore occlusion, while pores that are too large reduce surface area for cell adhesion[86]. The pore size for this project's scaffolds was around 700μm, which is large, but bound by the limits of our current printing technology. This pore size was necessary because decreasing it would require either a decrease in either strut width or porosity. Because strut width is dictated by the printhead and could not be lowered, and 70% porosity was important for fluid flow through the scaffold as previously discussed, the pore size could not be adjusted. In the future, alternate printheads or print methods could be used to reduce strut width and enable scaffold fabrication with smaller pores while retaining 70% porosity.

5.4. Bone Regeneration

Though some bone regeneration was observed post-mortem in Dog #3, no growth is currently observable on the radiographs of living patients. This is most surprising in Patient #1, who has had the device installed for approximately 24 weeks. While it is surprising to see no indications of osteogenesis in HAp scaffolds loaded with BMP, there are several reasons why this could have happened. The most likely cause is believed to be that the chemotherapy received by the patient in the 18 weeks following the surgery inhibited osteogenesis. Carboplatin, a standard of care for canines with osteosarcoma receiving adjuvant chemotherapy after amputation or limb spare, is an alkylating agent often used for the treatment of ovarian cancer in humans. Alkylating agents are highly reactive, and are meant to cause molecular changes to nucleic acids that result in mutagenic change or cell death[93]. Furthermore, Ehrhart et al. (2002)[94] performed a study examining the effects of cisplatin, a similar alkylating agent, on osteogenesis in dogs. In this study, negative effects including decreased mineralization volume, decreased osteoblast covered bone, and increased porosity were observed, though the effects were not determined to be clinically significant. It is possible that the adverse effects of this drug treatment counteracted the body's attempt to regrow bone, even when aided by the presence of the scaffold and rhBMP-2. While it is true that many studies have been performed using calcium phosphate scaffolds and BMP that saw excellent osteogenesis, few were performed on animals with active osteosarcoma who were undergoing chemotherapy. This is thought to be the main reason for the lack of growth in this trial. It is possible that patients will experience delayed osteogenesis after their 18 weeks of chemotherapy treatment, but his remains to be seen. It would be inadvisable to forgo administration of chemotherapy to these types of patients because adjuvant chemotherapy is associated with increased median survival time from just 4 months to 8-12 months[7].

Beyond carboplatin, several other potential reasons exist for the lack of osteogenesis. One factor that must be discussed is nutrient flow through the scaffold and the penetration of viable stem cells capable of initiating growth. The preliminary designs of the PCL sleeve were thought to help to direct flow through the scaffold towards the distal end, mimicking that of a natural bone. This was designed to "restore" the natural flow of the long bone, simulating the movement of bone marrow milieu through the medullary cavity. However, this design feature could have inadvertently restricted flow in some ways. First, because the aim was to direct flow along the length of the scaffold, the pores in Iterations 2 and 3 were quite small, only 5mm x 5mm. This could have inadvertently inhibited transcortical flow and restricted any interaction between the scaffold and the periosteum and surrounding soft tissue. If transcortical flow was excessively inhibited, too flow could have inadvertently been directed down the central canal, restricting flow to the perimeter of the gyroid.

Recent evidence has indicated that the periosteum plays a large role in the delivery of stem cells to the trauma site during bone regeneration[95]. Recently, periosteum-derived skeletal stem cells have been studied for their potential use in cell-based tissue engineering and have exhibited good *in vivo* bone formation potency[96]. Removal of portions of the periosteum is necessary for the installation of surgical fixation plates, so the portion at the overlap between the radius and sleeve/plate was removed for these procedures. By removing this portion and limiting transcortical flow with insufficient sleeve pore size, the potential contribution of the periosteum could have been severely limited. This could be potentially remedied via a channel/sleeve extension that allows interaction by the periosteum within the sleeve, which will be a future design consideration.

Another factor for consideration is the overall size of the defects. While a critical defect is typically defined to be approximately twice the diameter of the bone in length, the defects used in this clinical trial were super-critical, ranging from 11 to 14cm. This is another challenge of working with osteosarcoma patients, as they often require upwards of 40% of the bone's length to be removed. Because of the larger driving force needed, the size of these defects may have disrupted the flow regime, not allowing stem cells to as effectively penetrate the scaffold.

While unlikely, it is possible that lavage performed during surgery acted to "flush out" rhBMP from the scaffolds inner canal. Lavage is performed to remove blood/debris from the surgical site and involves flushing the area with sterile surgical fluid. However, for this action to have had a negative effect, the solution would have had to penetrate through the sleeve and scaffold and removed the BMP from the collagen sponge, all during the relatively short time that the entire device is installed before closing.

Finally, a yet unexplained development related to osteogenesis in clinical trial is the fibrous tissue formation on the outside of Dog #3's PCL sleeve. Because the patient was later confirmed to have local recurrence of the osteosarcoma, it is possible that the initial aspiration of this tissue resulted in a false negative. Benign ectopic bone formation as a result of the presence of rhBMP-2 has been observed in other studies but was consistently accompanied by prolific growth within the defect[37]. For the rhBMP-2 to have escaped sleeve to induce bone growth, it would need to have left the collagen sponge, moved through the scaffold, and out one of the 5mm x 5mm pores in the sleeve, only to form bone on PCL, which has a much more hydrophobic surface than HAp. While this cannot be ruled out, it remains unlikely given the apparent barriers to the growth factor's escape. One final possibility is that the presence of the sleeve triggered the formation of a biomembrane similar to that developed using the Masquelet technique. This technique involves

the placement of a cement spacer into a critical defect with the purpose of inducing the formation of a biomembrane. After the removal of the spacer, a graft is inserted and the membrane is intended to aid in osteogenesis and vascularization[97,98]. However, this biomembrane is known to become highly vascularized and secrete important growth factors, but not necessarily have the increased density that would appear on a radiograph. With recent histopathology results indicating that this tissue was bone and cartilage, this remains the least likely of the possibilities. This unexpected tissue proliferation remains an isolated incident, and has not been observed in any other patients.

Because this construct is the first of its kind, it is not known whether the sleeve had an ultimately negative effect on the scaffolds ability to facilitate osteogenesis. While the primary reason for the lack of bone growth is believed to be patient health and the presence of anti-cancer treatments, all the discussed possibilities should be considered as the device moves forward.

5.5. Methods for Improved Osteogenesis

If it is indeed true that chemotherapy is inhibiting osteogenesis, the idea of a delayed application of rhBMP-2 should be explored. This was not initially desired because delayed delivery of BMP has been shown to result in lower bone density[99]. However, it is still thought to be favorable compared to the total absence of BMP[100]. This would also limit the possible delivery methods for the BMP. It would no longer be possible to use an collagen sponge, as the thin collagen matrix would degrade before the growth factor would be delivered. However, some studies have seen success by adding the BMP directly via injection of polymer carriers containing growth factors[101]. This means that a delayed delivery of rhBMP-2 could take the form of an injection through the sleeve into the scaffold, after carboplatin treatment is completed. Existing pores in the sleeve could be used to guide the needle into the central canal to deliver BMP.

Opening the sides of the sleeve to expose the scaffold to more natural tissue was a design choice implemented in Iteration 4, and it remains to be seen whether this will improve bone regeneration. It is expected to increase transcortical flow and interactions between the scaffold and the periosteum and soft tissues. The transition to β-TCP scaffolds is predicted have a favorable effect on osteogenesis. While HAp is a proven bone TE material and the primary mineral component of bone, TCP has proven slightly better in terms of osteogenesis and biodegradation because osteoblasts are able to replace the scaffold material with natural bone faster[89,102]. With the recent development of a β-TCP photocasting slurry, scaffolds of the same morphology can now be manufactured with the more osteogenic material. While lavage is unlikely to contributed towards loss of BMP in the system, it is to be performed minimally after the sleeve is installed in the future to reduce any risk of flushing away important growth factor. With the newest design exposing the scaffold much more to the surgical cavity, this has become more critical.

6. Conclusion

6.1. Summary of Work

A novel method for the fixation and protection of a brittle but osteogenic bone tissue engineering scaffold has been developed and tested, both *ex vivo* and in a pilot canine clinical trial. The construct is mechanically sound, having demonstrated no scaffold failure when tested under anatomical load or when viewed on radiographs of devices installed in patients for 24 weeks to date and continuing. Based on experience and clinician feedback, a much thinner device was developed with easier installation and improved patient comfort as design goals. Patient-specific gyroid scaffolds have shown permeability values comparable to that of trabecular bone, indicating good conditions for the migration of the cells, exchange of nutrients needed for

osteogenesis, and removal of waste. These can be manufactured using hydroxyapatite and β-tricalcium phosphate which, while brittle in nature, have been shown to remain immobilized and intact within the defects as a result of their enclosure in the PCL sleeves.

Full devices installed in clinical trial patients have shown to be simple to install, and although initial designs were bulky, patients were able to successfully recover weight-bearing ability and their natural gates. Unfortunately, regeneration of bone within the defects of critical trial patients has only been sparsely observed. Multiple factors are thought to be responsible for this lack of osteogenesis in the first 12-24 weeks. We believe the most likely cause of the inhibition to growth caused by chemotherapy treatment. Some growth was observed postmortem at the distal transition zone in the only patient to pass away thus far, but radiographic evidence of bone growth is not observable in living patients.

6.2. Significance

With this technology, polymer additives are not needed to strengthen bioceramic scaffolds for their use in bone tissue engineering. Instead, a patient-specific support sleeve can be used so that the scaffold is uninhibited by the additives hindering its osteoconduction, and degradation. The technology allows engineers to return to the best possible materials for osteogenesis, some of which may have been ruled out due to their brittle nature. The device is easily installable and can be installed without disrupting the standard limb-salvaging procedure. It is custom designed for each patient and has potential application in a large range of defects (epiphyseal, diaphyseal, mandibular, etc.). Its efficacy in protecting brittle scaffolds is proven, opening the door for its use with the most osteoconductive scaffolds possible. State of the art studies have shown that the removal of metal fixation components is possible within a 1-year timeframe[21]. Therefore, no

metal would remain in the body after 1 year, and no PCL would remain after approximately 2 years, leaving fully regenerated, natural bone.

6.3. Future Directions

While this device is very promising, a continuation of the constant cycle of testing and improvement is needed for its optimization. A related project was recently completed that used finite-element analysis (FEA) to consider various alternative designs. Incorporation of these discoveries into this work will be fruitful. Ideal mechanical and biological characteristics for this device will be achieved through continued study of trial patients, FEA, and mechanical testing. Most recently, the much thinner 4th iteration of the sleeve was successfully installed into a patient using a β-TCP scaffold. Further mechanical and biological improvement could be brought to the scaffold in the form of dopants, which can improve these properties while keeping the scaffold fully degradable. Additives like magnesium MgO, SrO, and SiO_2 doped into β-TCP have shown very promising results[103].

Further testing would also allow even better characterization of the device. As previously discussed, further study with a more precise pressure transducer is needed to understand permeability at specific scaffold morphology and anatomical flow conditions. Repeat bend and construct testing with the newer iterations of the sleeve would help further detail how the construct behaves as a whole. These results can feed into new generations of the FEA discussed above. Finally, a controlled animal study or clinical trauma study would confirm whether bone growth was completely inhibited by anti-cancer agents. A newer study could also incorporate the periosteum into the device to enable contribution of its skeletal stem cells.

Far down the road, this device could be coupled with bioabsorbable fixations to create an entire construct that is installed, conducts osteogenesis to achieve full bridging of the defect and union

with the native bone, naturally degrades, and no downstream invasive surgery is needed for removal. With this end goal in mind, the development of constructs such as this to reinforce tissue engineering scaffolds is a step in the right direction.

References

(1) Roddy, E.; DeBaun, M. R.; Daoud-Gray, A.; Yang, Y. P.; Gardner, M. J. Treatment of Critical-Sized Bone Defects: Clinical and Tissue Engineering Perspectives. *Eur. J. Orthop. Surg. Traumatol. Orthop. Traumatol.* **2018**, *28* (3), 351–362. https://doi.org/10.1007/s00590-017-2063-0.

(2) Nauth, A.; McKee, M. D.; Einhorn, T. A.; Watson, J. T.; Li, R.; Schemitsch, E. H. Managing Bone Defects. *J. Orthop. Trauma* **2011**, *25* (8), 462–466. https://doi.org/10.1097/BOT.0b013e318224caf0.

(3) Liptak, J. M.; Dernell, W. S.; Ehrhart, N.; Withrow, S. J. Canine Appendicular Osteosarcoma: Diagnosis and Palliative Treatment. **2004**, 9.

(4) MacDonald, T. L.; Schiller, T. D. Limb-Sparing Surgery Using Tantalum Metal Endoprosthesis in a Dog with Osteosarcoma of the Distal Radius. *Can. Vet. J.* **2010**, *51* (5), 497–500.

(5) Szewczyk, M.; Lechowski, R.; Zabielska, K. What Do We Know about Canine Osteosarcoma Treatment? – Review. *Vet. Res. Commun.* **2015**, *39* (1), 61–67. https://doi.org/10.1007/s11259-014-9623-0.

(6) Schmidt, A. F.; Nielen, M.; Klungel, O. H.; Hoes, A. W.; de Boer, A.; Groenwold, R. H. H.; Kirpensteijn, J. Prognostic Factors of Early Metastasis and Mortality in Dogs with Appendicular Osteosarcoma after Receiving Surgery: An Individual Patient Data Meta-Analysis. *Prev. Vet. Med.* **2013**, *112* (3), 414–422. https://doi.org/10.1016/j.prevetmed.2013.08.011.

(7) McMahon, M.; Mathie, T.; Stingle, N.; Romansik, E.; Vail, D.; London, C. Adjuvant Carboplatin and Gemcitabine Combination Chemotherapy Postamputation in Canine Appendicular Osteosarcoma. *J. Vet. Intern. Med.* **2011**, *25* (3), 511–517. https://doi.org/10.1111/j.1939-1676.2011.0697.x.

(8) Withrow, S. J. *Withrow and MacEwen's Small Animal Clinical Oncology*; Elsevier Health Sciences, 2007.

(9) Morello, E.; Vasconi, E.; Martano, M.; Peirone, B.; Buracco, P. Pasteurized Tumoral Autograft and Adjuvant Chemotherapy for the Treatment of Canine Distal Radial Osteosarcoma: 13 Cases. *Vet. Surg.* **2003**, *32* (6), 539–544. https://doi.org/10.1111/j.1532-950X.2003.00539.x.

(10) Buracco, P.; Morello, E.; Martano, M.; Vasconi, M. E. Pasteurized Tumoral Autograft as a Novel Procedure for Limb Sparing in the Dog: A Clinical Report. *Vet. Surg. VS* **2002**, *31* (6), 525–532. https://doi.org/10.1053/jvet.2002.34674.

(11) *Animal Surgical Center of Michigan - Veterinarian in Flint, MI*. https://www.animalsurgicalcenter.com/limb-spare-surgery-for-bone-cancer (accessed 2022-01-10).

(12) Gasch, E. G.; Rivier, P.; Bardet, J. F. Free Proximal Cortical Ulnar Autograft for the Treatment of Distal Radial Osteosarcoma in a Dog. *Can. Vet. J.* **2013**, *54* (2), 162–166.

(13) Liptak, J. M.; Dernell, W. S.; Ehrhart, N.; Lafferty, M. H.; Monteith, G. J.; Withrow, S. J. Cortical Allograft and Endoprosthesis for Limb-Sparing Surgery in Dogs with Distal Radial Osteosarcoma: A Prospective Clinical Comparison of Two Different Limb-Sparing Techniques. *Vet. Surg.* **2006**, *35* (6), 518–533. https://doi.org/10.1111/j.1532-950X.2006.00185.x.

(14) Jacobsen, G.; Easter, D. Allograft vs. Xenograft: Practical Considerations for Biologic Scaffolds.

(15) admin. *Development of an intramuscular xenograft model of canine osteosarcoma in mice for evaluation of the effects of radiation therapy.* OrthoVetSuperSite. https://www.orthovetsupersite.org/abstract/development-intramuscular-xenograft-model-canine-osteosarcoma-mice-evaluation-effects (accessed 2022-01-10).

(16) Séguin, B.; Walsh, P. J.; Mason, D. R.; Wisner, E. R.; Parmenter, J. L.; Dernell, W. S. Use of An Ipsilateral Vascularized Ulnar Transposition Autograft for Limb-Sparing Surgery of the Distal Radius in Dogs: An Anatomic and Clinical Study. *Vet. Surg.* **2003**, *32* (1), 69–79. https://doi.org/10.1053/jvet.2003.50003.

(17) Pelker, R. R.; Friedlaender, G. E.; Markham, T. C. Biomechanical Properties of Bone Allografts. *Clin. Orthop.* **1983**, No. 174, 54–57.

(18) Stevenson, S. The Immune Response to Osteochondral Allografts in Dogs. *JBJS* **1987**, *69* (4), 573–582.

(19) Holmes, R. E.; Bucholz, R. W.; Mooney, V. Porous Hydroxyapatite as a Bone Graft Substitute in Diaphyseal Defects: A Histometric Study. *J. Orthop. Res.* **1987**, *5* (1), 114–121. https://doi.org/10.1002/jor.1100050114.

(20) Kattimani, V. S.; Kondaka, S.; Lingamaneni, K. P. Hydroxyapatite–-Past, Present, and Future in Bone Regeneration. *Bone Tissue Regen. Insights* **2016**, *7*, BTRI.S36138. https://doi.org/10.4137/BTRI.S36138.

(21) Franch, J.; Barba, A.; Rappe, K.; Maazouz, Y.; Ginebra, M. Use of Three-dimensionally Printed B-tricalcium Phosphate Synthetic Bone Graft Combined with Recombinant Human Bone Morphogenic Protein-2 to Treat a Severe Radial Atrophic Nonunion in a Yorkshire Terrier. *Vet. Surg.* **2020**, vsu.13476. https://doi.org/10.1111/vsu.13476.

(22) Akagi, H.; Ochi, H.; Soeta, S.; Kanno, N.; Yoshihara, M.; Okazaki, K.; Yogo, T.; Harada, Y.; Amasaki, H.; Hara, Y. A Comparison of the Process of Remodeling of Hydroxyapatite/Poly-D/L-Lactide and Beta-Tricalcium Phosphate in a Loading Site. *BioMed Res. Int.* **2015**, *2015*, 730105. https://doi.org/10.1155/2015/730105.

(23) Yang, Y. P.; Labus, K. M.; Gadomski, B. C.; Bruyas, A.; Easley, J.; Nelson, B.; Palmer, R. H.; McGilvray, K.; Regan, D.; Puttlitz, C. M.; Stahl, A.; Lui, E.; Li, J.; Moeinzadeh, S.; Kim, S.; Maloney, W.; Gardner, M. J. Osteoinductive 3D Printed Scaffold Healed 5 Cm Segmental Bone Defects in the Ovine Metatarsus. *Sci. Rep.* **2021**, *11* (1), 6704. https://doi.org/10.1038/s41598-021-86210-5.

(24) Choi, S.; Oh, Y.-I.; Park, K.-H.; Lee, J.-S.; Shim, J.-H.; Kang, B.-J. New Clinical Application of Three-Dimensional-Printed Polycaprolactone/β-Tricalcium Phosphate Scaffold as an Alternative to Allograft Bone for Limb-Sparing Surgery in a Dog with Distal Radial Osteosarcoma. *J. Vet. Med. Sci.* **2019**, *81* (3), 434–439. https://doi.org/10.1292/jvms.18-0158.

(25) Ishack, S.; Mediero, A.; Wilder, T.; Ricci, J. L.; Cronstein, B. N. Bone Regeneration in Critical Bone Defects Using Three-Dimensionally Printed β-Tricalcium Phosphate/Hydroxyapatite Scaffolds Is Enhanced by Coating Scaffolds with Either Dipyridamole or BMP-2: AGENTS THAT STIMULATE A2A RECEPTORS FURTHER ENHANCE HA/B-TCP SCAFFOLDS BONE REGENERATION. *J. Biomed. Mater. Res. B Appl. Biomater.* **2017**, *105* (2), 366–375. https://doi.org/10.1002/jbm.b.33561.

(26) Isaacson, N.; Lopez-Ambrosio, K.; Chubb, L.; Waanders, N.; Hoffmann, E.; Witt, C.; James, S.; Prawel, D. A. Compressive Properties and Failure Behavior of Photocast

Hydroxyapatite Gyroid Scaffolds Vary with Porosity. *J. Biomater. Appl.* **2022**, 08853282211073904. https://doi.org/10.1177/08853282211073904.

(27) Koski, C.; Onuike, B.; Bandyopadhyay, A.; Bose, S. Starch-Hydroxyapatite Composite Bone Scaffold Fabrication Utilizing a Slurry Extrusion-Based Solid Freeform Fabricator. *Addit. Manuf.* **2018**, *24*, 47–59. https://doi.org/10.1016/j.addma.2018.08.030.

(28) Huang, B.; Caetano, G.; Vyas, C.; Blaker, J.; Diver, C.; Bártolo, P. Polymer-Ceramic Composite Scaffolds: The Effect of Hydroxyapatite and β-Tri-Calcium Phosphate. *Materials* **2018**, *11* (1), 129. https://doi.org/10.3390/ma11010129.

(29) Lu, L.; Zhang, Q.; Wootton, D.; Chiou, R.; Li, D.; Lu, B.; Lelkes, P.; Zhou, J. Biocompatibility and Biodegradation Studies of PCL/β-TCP Bone Tissue Scaffold Fabricated by Structural Porogen Method. *J. Mater. Sci. Mater. Med.* **2012**, *23* (9), 2217–2226. https://doi.org/10.1007/s10856-012-4695-2.

(30) Chen, D.; Zhao, M.; Mundy, G. R. Bone Morphogenetic Proteins. *Growth Factors Chur Switz.* **2004**, *22* (4), 233–241. https://doi.org/10.1080/08977190412331279890.

(31) Zhu, L.; Liu, Y.; Wang, A.; Zhu, Z.; Li, Y.; Zhu, C.; Che, Z.; Liu, T.; Liu, H.; Huang, L. Application of BMP in Bone Tissue Engineering. *Front. Bioeng. Biotechnol.* **2022**, *10*.

(32) Conway, J. D.; Shabtai, L.; Bauernschub, A.; Specht, S. C. BMP-7 Versus BMP-2 for the Treatment of Long Bone Nonunion. *Orthopedics* **2014**, *37* (12), e1049–e1057. https://doi.org/10.3928/01477447-20141124-50.

(33) *BMP-2 and BMP-7 continue to show success in long bone fractures and nonunions*. https://www.healio.com/news/orthopedics/20120325/bmp-2-and-bmp-7-continue-to-show-success-in-long-bone-fractures-and-nonunions (accessed 2022-05-16).

(34) Wozney, J. M.; Rosen, V.; Celeste, A. J.; Mitsock, L. M.; Whitters, M. J.; al, et. Novel Regulators of Bone Formation: Molecular Clones and Activites. *Science* **1988**, *242* (4885), 1528.

(35) Boyce, A. S.; Reveal, G.; Scheid, D. K.; Kaehr, D. M.; Maar, D.; Watts, M.; Stone, M. B. Canine Investigation of RhBMP-2, Autogenous Bone Graft, and RhBMP-2 With Autogenous Bone Graft for the Healing of a Large Segmental Tibial Defect. *J. Orthop. Trauma* **2009**, *23* (10), 685–692. https://doi.org/10.1097/BOT.0b013e3181a10378.

(36) Kinoshita, A.; Oda, S.; Takahashi, K.; Yokota, S.; Ishikawa, I. Periodontal Regeneration by Application of Recombinant Human Bone Morphogenetic Protein-2 to Horizontal Circumferential Defects Created by Experimental Periodontitis in Beagle Dogs. *J. Periodontol.* **1997**, *68* (2), 103–109. https://doi.org/10.1902/jop.1997.68.2.103.

(37) Milovancev, M.; Muir, P.; Manley, P. A.; Seeherman, H. J.; Schaefer, S. Clinical Application of Recombinant Human Bone Morphogenetic Protein-2 in 4 Dogs. *Vet. Surg.* **2007**, *36* (2), 132–140. https://doi.org/10.1111/j.1532-950X.2007.00245.x.

(38) *Development - BMP signaling Pathway Map - PrimePCR | Life Science | Bio-Rad*. https://commerce.bio-rad.com/en-uk/prime-pcr-assays/pathway/apoptosis-survival/development-bmp-signaling (accessed 2022-01-03).

(39) Zegzula, H. D.; Buck, D. C.; Brekke, J.; Wozney, J. M.; Hollinger, J. O. Bone Formation with Use of RhBMP-2 (Recombinant Human Bone Morphogenetic Protein-2). *J. Bone Joint Surg. Am.* **1997**, *79* (12), 1778–1790. https://doi.org/10.2106/00004623-199712000-00003.

(40) Boudrieau, R. Initial Experience With RhBMP-2 Delivered in a Compressive Resistant Matrix for Mandibular Reconstruction in 5 Dogs. *Vet Surg* **2015**, *44*, 443–458.

(41) Jun, S.-H.; Lee, E.-J.; Jang, T.-S.; Kim, H.-E.; Jang, J.-H.; Koh, Y.-H. Bone Morphogenic Protein-2 (BMP-2) Loaded Hybrid Coating on Porous Hydroxyapatite Scaffolds for Bone Tissue Engineering. *J. Mater. Sci. Mater. Med.* **2013**, *24* (3), 773–782. https://doi.org/10.1007/s10856-012-4822-0.

(42) Dong, X.; Wang, Q.; Wu, T.; Pan, H. Understanding Adsorption-Desorption Dynamics of BMP-2 on Hydroxyapatite (001) Surface. *Biophys. J.* **2007**, *93* (3), 750–759. https://doi.org/10.1529/biophysj.106.103168.

(43) Pinel, C. B.; Pluhar, G. E. Clinical Application of Recombinant Human Bone Morphogenetic Protein in Cats and Dogs: A Review of 13 Cases. *53*, 8.

(44) Massie, A. M.; Kapatkin, A. S.; Fuller, M. C.; Verstraete, F. J. M.; Arzi, B. Outcome of Nonunion Fractures in Dogs Treated with Fixation, Compression Resistant Matrix, and Recombinant Human Bone Morphogenetic Protein-2. *Vet. Comp. Orthop. Traumatol.* **2017**, *30* (2), 153–159. https://doi.org/10.3415/VCOT-16-05-0082.

(45) Fogden, A.; Hyde, S. T. Parametrization of Triply Periodic Minimal Surfaces. I. Mathematical Basis of the Construction Algorithm for the Regular Class. *Acta Crystallogr. A* **1992**, *48* (4), 442–451. https://doi.org/10.1107/S0108767391015167.

(46) Bobbert, F. S. L.; Lietaert, K.; Eftekhari, A. A.; Pouran, B.; Ahmadi, S. M.; Weinans, H.; Zadpoor, A. A. Additively Manufactured Metallic Porous Biomaterials Based on Minimal Surfaces: A Unique Combination of Topological, Mechanical, and Mass Transport Properties. *Acta Biomater.* **2017**, *53*, 572–584. https://doi.org/10.1016/j.actbio.2017.02.024.

(47) Asbai-Ghoudan, R.; Ruiz de Galarreta, S.; Rodriguez-Florez, N. Analytical Model for the Prediction of Permeability of Triply Periodic Minimal Surfaces. *J. Mech. Behav. Biomed. Mater.* **2021**, *124*, 104804. https://doi.org/10.1016/j.jmbbm.2021.104804.

(48) Ritz, U.; Gerke, R.; Götz, H.; Stein, S.; Rommens, P. M. A New Bone Substitute Developed from 3D-Prints of Polylactide (PLA) Loaded with Collagen I: An In Vitro Study. *Int. J. Mol. Sci.* **2017**, *18* (12), 2569. https://doi.org/10.3390/ijms18122569.

(49) Shi, X.; Liao, W.; Li, P.; Zhang, C.; Liu, T.; Wang, C.; Wu, J. Comparison of Compression Performance and Energy Absorption of Lattice Structures Fabricated by Selective Laser Melting. *Adv. Eng. Mater.* **2020**, *22* (11), 2000453. https://doi.org/10.1002/adem.202000453.

(50) Caiazzo, F.; Alfieri, V.; Bujazha, B. D. Additive Manufacturing of Biomorphic Scaffolds for Bone Tissue Engineering. *Int. J. Adv. Manuf. Technol.* **2021**, *113* (9), 2909–2923. https://doi.org/10.1007/s00170-021-06773-5.

(51) Liu, F.; Ran, Q.; Zhao, M.; Zhang, T.; Zhang, D. Z.; Su, Z. Additively Manufactured Continuous Cell-Size Gradient Porous Scaffolds: Pore Characteristics, Mechanical Properties and Biological Responses In Vitro. *Materials* **2020**, *13* (11), 2589. https://doi.org/10.3390/ma13112589.

(52) 2 - The Basic Properties of Building Materials. In *Building Materials in Civil Engineering*; Zhang, H., Ed.; Woodhead Publishing Series in Civil and Structural Engineering; Woodhead Publishing, 2011; pp 7–423. https://doi.org/10.1533/9781845699567.7.

(53) Santos, J.; Pires, T.; Gouveia, B. P.; Castro, A. P. G.; Fernandes, P. R. On the Permeability of TPMS Scaffolds. *J. Mech. Behav. Biomed. Mater.* **2020**, *110*, 103932. https://doi.org/10.1016/j.jmbbm.2020.103932.

(54) Dias, M. R.; Fernandes, P. R.; Guedes, J. M.; Hollister, S. J. Permeability Analysis of Scaffolds for Bone Tissue Engineering. *J. Biomech.* **2012**, *45* (6), 938–944. https://doi.org/10.1016/j.jbiomech.2012.01.019.

(55) Mitsak, A. G.; Kemppainen, J. M.; Harris, M. T.; Hollister, S. J. Effect of Polycaprolactone Scaffold Permeability on Bone Regeneration In Vivo. *Tissue Eng. Part A* **2011**, *17* (13–14), 1831–1839. https://doi.org/10.1089/ten.tea.2010.0560.

(56) Park, J. Y.; Park, S. H.; Kim, M. G.; Park, S.-H.; Yoo, T. H.; Kim, M. S. Biomimetic Scaffolds for Bone Tissue Engineering. In *Biomimetic Medical Materials: From Nanotechnology to 3D Bioprinting*; Noh, I., Ed.; Advances in Experimental Medicine and Biology; Springer: Singapore, 2018; pp 109–121. https://doi.org/10.1007/978-981-13-0445-3_7.

(57) Wu, S.; Liu, X.; Yeung, K. W. K.; Liu, C.; Yang, X. Biomimetic Porous Scaffolds for Bone Tissue Engineering. *Mater. Sci. Eng. R Rep.* **2014**, *80*, 1–36. https://doi.org/10.1016/j.mser.2014.04.001.

(58) Papastavrou, E.; Breedon, P.; Fairhurst, D. Low-Temperature Deposition Modeling of β-TCP Scaffolds with Controlled Bimodal Porosity. In *Biomaterials for Tissue Engineering: Methods and Protocols*; Chawla, K., Ed.; Methods in Molecular Biology; Springer: New York, NY, 2018; pp 41–54. https://doi.org/10.1007/978-1-4939-7741-3_4.

(59) Li, J.; Yuan, H.; Chandrakar, A.; Moroni, L.; Habibovic, P. 3D Porous Ti6Al4V-Beta-Tricalcium Phosphate Scaffolds Directly Fabricated by Additive Manufacturing. *Acta Biomater.* **2021**, *126*, 496–510. https://doi.org/10.1016/j.actbio.2021.03.021.

(60) Olivares, A. L.; Marsal, È.; Planell, J. A.; Lacroix, D. Finite Element Study of Scaffold Architecture Design and Culture Conditions for Tissue Engineering. *Biomaterials* **2009**, *30* (30), 6142–6149. https://doi.org/10.1016/j.biomaterials.2009.07.041.

(61) Cheng, A.; Schwartz, Z.; Kahn, A.; Li, X.; Shao, Z.; Sun, M.; Ao, Y.; Boyan, B. D.; Chen, H. Advances in Porous Scaffold Design for Bone and Cartilage Tissue Engineering and Regeneration. *Tissue Eng. Part B Rev.* **2019**, *25* (1), 14–29. https://doi.org/10.1089/ten.teb.2018.0119.

(62) Luo, J.-W.; Chen, L.; Min, T.; Shan, F.; Kang, Q.; Tao, W. Macroscopic Transport Properties of Gyroid Structures Based on Pore-Scale Studies: Permeability, Diffusivity and Thermal Conductivity. *Int. J. Heat Mass Transf.* **2020**, *146*, 118837. https://doi.org/10.1016/j.ijheatmasstransfer.2019.118837.

(63) Grimm, M. J.; Williams, J. L. Measurements of Permeability in Human Calcaneal Trabecular Bone. *J. Biomech.* **1997**, *30* (7), 743–745. https://doi.org/10.1016/S0021-9290(97)00016-X.

(64) Pires, T.; Santos, J.; Ruben, R. B.; Gouveia, B. P.; Castro, A. P. G.; Fernandes, P. R. Numerical-Experimental Analysis of the Permeability-Porosity Relationship in Triply Periodic Minimal Surfaces Scaffolds. *J. Biomech.* **2021**, *117*, 110263. https://doi.org/10.1016/j.jbiomech.2021.110263.

(65) Pfaffinger, M.; Hartmann, M.; Schwentenwein, M.; Stampfl, J. Stabilization of Tricalcium Phosphate Slurries against Sedimentation for Stereolithographic Additive Manufacturing and Influence on the Final Mechanical Properties. *Int. J. Appl. Ceram. Technol.* **2017**, *14* (4), 499–506. https://doi.org/10.1111/ijac.12664.

(66) Lopez Ambrosio, Katherine V. HYDROXYAPATITE STRUCTURES CREATED BY ADDITIVE MANUFACTURING WITH EXTRUDED PHOTOPOLYMER. Master's Thesis, Colorado State University, Ft. Collins, CO, 2019.

(67) Bartnikowski, M.; Dargaville, T. R.; Ivanovski, S.; Hutmacher, D. W. Degradation Mechanisms of Polycaprolactone in the Context of Chemistry, Geometry and Environment. *Prog. Polym. Sci.* **2019**, *96*, 1–20. https://doi.org/10.1016/j.progpolymsci.2019.05.004.

(68) Woodruff, M. A.; Hutmacher, D. W. The Return of a Forgotten Polymer—Polycaprolactone in the 21st Century. *Prog. Polym. Sci.* **2010**, *35* (10), 1217–1256. https://doi.org/10.1016/j.progpolymsci.2010.04.002.

(69) Ko, J.; Mohtaram, N. K.; Ahmed, F.; Montgomery, A.; Carlson, M.; Lee, P. C. D.; Willerth, S. M.; Jun, M. B. G. Fabrication of Poly (ε-Caprolactone) Microfiber Scaffolds with Varying Topography and Mechanical Properties for Stem Cell-Based Tissue Engineering Applications. *J. Biomater. Sci. -- Polym. Ed.* **2014**, *25* (1), 1–17. https://doi.org/10.1080/09205063.2013.830913.

(70) Chen, J.-M.; Lee, D.; Yang, J.-W.; Sheng-Han, L.; Yu-Ting, L.; Shih-Jung, L.; Shih-Jung, L. Solution Extrusion Additive Manufacturing of Biodegradable Polycaprolactone. *Appl. Sci.* **2020**, *10* (9), 3189. http://dx.doi.org.ezproxy2.library.colostate.edu/10.3390/app10093189.

(71) Marrazzo, C.; Maio, E. D.; Iannace, S. Conventional and Nanometric Nucleating Agents in Poly(ε-Caprolactone) Foaming: Crystals vs. Bubbles Nucleation. *Polym. Eng. Sci.* **2008**, *48* (2), 336–344. https://doi.org/10.1002/pen.20937.

(72) Ceretti, E.; Ginestra, P.; Neto, P. I.; Fiorentino, A.; Da Silva, J. V. L. Multi-Layered Scaffolds Production via Fused Deposition Modeling (FDM) Using an Open Source 3D Printer: Process Parameters Optimization for Dimensional Accuracy and Design Reproducibility. *Procedia CIRP* **2017**, *65*, 13–18. https://doi.org/10.1016/j.procir.2017.04.042.

(73) Sun, H.; Mei, L.; Song, C.; Cui, X.; Wang, P. The in Vivo Degradation, Absorption and Excretion of PCL-Based Implant. *Biomaterials* **2006**, *27* (9), 1735–1740. https://doi.org/10.1016/j.biomaterials.2005.09.019.

(74) Rydz, J.; Sikorska, W.; Kyulavska, M.; Christova, D. Polyester-Based (Bio)Degradable Polymers as Environmentally Friendly Materials for Sustainable Development. *Int. J. Mol. Sci.* **2015**, *16* (1), 564–596. https://doi.org/10.3390/ijms16010564.

(75) Pitt, C. G.; Chasalow, F. I.; Hibionada, Y. M.; Klimas, D. M.; Schindler, A. Aliphatic Polyesters. I. The Degradation of Poly(ε-Caprolactone) in Vivo. *J. Appl. Polym. Sci.* **1981**, *26* (11), 3779–3787. https://doi.org/10.1002/app.1981.070261124.

(76) Gupta, S.; Bit, A. 16 - Rapid Prototyping for Polymeric Gels. In *Polymeric Gels*; Pal, K., Banerjee, I., Eds.; Woodhead Publishing Series in Biomaterials; Woodhead Publishing, 2018; pp 397–439. https://doi.org/10.1016/B978-0-08-102179-8.00016-8.

(77) *InVesalius*. https://invesalius.github.io/about.html (accessed 2021-12-07).

(78) Ambrosio, K. V. L. HYDROXYAPATITE STRUCTURES CREATED BY ADDITIVE MANUFACTURING WITH EXTRUDED PHOTOPOLYMER, Colorado State University, Fort Collins, CO, 2019.

(79) *Peracetic Acid Sterilization | Disinfection & Sterilization Guidelines | Guidelines Library | Guidelines Library | Infection Control | CDC*. https://www.cdc.gov/infectioncontrol/guidelines/disinfection/sterilization/peracetic-acid.html (accessed 2022-06-14).

(80) Castro; Pires; Santos; Gouveia; Fernandes. Permeability versus Design in TPMS Scaffolds. *Materials* **2019**, *12* (8), 1313. https://doi.org/10.3390/ma12081313.

(81) Burton, N. J.; Dobney, J. A.; Owen, M. R.; Colborne, G. R. Joint Angle, Moment and Power Compensations in Dogs with Fragmented Medial Coronoid Process. *Vet. Comp. Orthop. Traumatol.* **2008**, *21* (02), 110–118. https://doi.org/10.3415/VCOT-07-04-0038.

(82) Kirpensteijn, J.; van den Bos, R.; van den Brom, W. E.; Hazewinkel, H. a. W. Ground Reaction Force Analysis of Large Breed Dogs When Walking after the Amputation of a Limb. *Vet. Rec.* **2000**, *146* (6), 155–159. https://doi.org/10.1136/vr.146.6.155.

(83) Budsberg, S. C.; Verstraete, M. C.; Soutas-Little, R. W. Force Plate Analysis of the Walking Gait in Healthy Dogs. *Am. J. Vet. Res.* **1987**, *48* (6), 915–918.

(84) Riggs, C. M.; DeCamp, C. E.; Soutas-Little, R. W.; Braden, T. D.; Richter, M. A. Effects of Subject Velocity on Force Plate-Measured Ground Reaction Forces in Healthy Greyhounds at the Trot. *Am. J. Vet. Res.* **1993**, *54* (9), 1523–1526.

(85) Pooya, H. A.; Seguin, B.; Mason, D. R.; Walsh, P. J.; Taylor, K. T.; Kass, P. H.; Stover, S. M. Biomechanical Comparison of Cortical Radial Graft versus Ulnar Transposition Graft Limb-Sparing Techniques for the Distal Radial Site in Dogs. *Vet. Surg.* **2004**, *33* (4), 301–308. https://doi.org/10.1111/j.1532-950X.2004.04044.x.

(86) Zaharin, H. A.; Abdul Rani, A. M.; Azam, F. I.; Ginta, T. L.; Sallih, N.; Ahmad, A.; Yunus, N. A.; Zulkifli, T. Z. A. Effect of Unit Cell Type and Pore Size on Porosity and Mechanical Behavior of Additively Manufactured Ti6Al4V Scaffolds. *Materials* **2018**, *11* (12), 2402. https://doi.org/10.3390/ma11122402.

(87) Liptak, J. M.; Ehrhart, N.; Santoni, B. G.; Wheeler, D. L. Cortical Bone Graft and Endoprosthesis in the Distal Radius of Dogs: A Biomechanical Comparison of Two Different Limb-Sparing Techniques. *Vet. Surg.* **2006**, *35* (2), 150–160. https://doi.org/10.1111/j.1532-950X.2006.00126.x.

(88) Kano, W. T.; Rahal, S. C.; Agostinho, F. S.; Mesquita, L. R.; Santos, R. R.; Monteiro, F. O. B.; Castilho, M. S.; Melchert, A. Kinetic and Temporospatial Gait Parameters in a Heterogeneous Group of Dogs. *BMC Vet. Res.* **2016**, *12* (1), 2. https://doi.org/10.1186/s12917-015-0631-2.

(89) Onodera, J.; Kondo, E.; Omizu, N.; Ueda, D.; Yagi, T.; Yasuda, K. Beta-Tricalcium Phosphate Shows Superior Absorption Rate and Osteoconductivity Compared to Hydroxyapatite in Open-Wedge High Tibial Osteotomy. *Knee Surg. Sports Traumatol. Arthrosc. Off. J. ESSKA* **2014**, *22* (11), 2763–2770. https://doi.org/10.1007/s00167-013-2681-y.

(90) Wazen, R. M.; Currey, J. A.; Guo, H.; Brunski, J. B.; Helms, J. A.; Nanci, A. Micromotion-Induced Strain Fields Influence Early Stages of Repair at Bone–Implant Interfaces. *Acta Biomater.* **2013**, *9* (5), 6663–6674. https://doi.org/10.1016/j.actbio.2013.01.014.

(91) Garg, P.; Mazur, M. M.; Buck, A. C.; Wandtke, M. E.; Liu, J.; Ebraheim, N. A. Prospective Review of Mesenchymal Stem Cells Differentiation into Osteoblasts. *Orthop. Surg.* **2017**, *9* (1), 13–19. https://doi.org/10.1111/os.12304.

(92) Vorys, G. C.; Bai, H.; Chandhanayingyong, C.; Lee, C. H.; Compton, J. T.; Caldwell, J.-M.; Gardner, T. R.; Mao, J. J.; Lee, F. Y. Optimal Internal Fixation of Anatomically Shaped Synthetic Bone Grafts for Massive Segmental Defects of Long Bones. *Clin. Biomech.* **2015**, *30* (10), 1114–1118. https://doi.org/10.1016/j.clinbiomech.2015.08.016.

(93) The Editors of Encyclopaedia Brittanica. Alkylating Agent | Chemical Compound. *Encyclopaedia Brittanica*; 2017.

(94) Ehrhart, N.; Eurell, J. A. C.; Tommasini, M.; Constable, P. D.; Johnson, A. L.; Feretti, A. Effect of Cisplatin on Bone Transport Osteogenesis in Dogs. *Am. J. Vet. Res.* **2002**, *63* (5), 703–711. https://doi.org/10.2460/ajvr.2002.63.703.

(95) Duchamp de Lageneste, O.; Julien, A.; Abou-Khalil, R.; Frangi, G.; Carvalho, C.; Cagnard, N.; Cordier, C.; Conway, S. J.; Colnot, C. Periosteum Contains Skeletal Stem Cells with

High Bone Regenerative Potential Controlled by Periostin. *Nat. Commun.* **2018**, *9* (1), 773. https://doi.org/10.1038/s41467-018-03124-z.

(96) Groeneveldt, L. C.; Herpelinck, T.; Maréchal, M.; Politis, C.; van IJcken, W. F. J.; Huylebroeck, D.; Geris, L.; Mulugeta, E.; Luyten, F. P. The Bone-Forming Properties of Periosteum-Derived Cells Differ Between Harvest Sites. *Front. Cell Dev. Biol.* **2020**, *8*.

(97) Wong, T. M.; Lau, T. W.; Li, X.; Fang, C.; Yeung, K.; Leung, F. Masquelet Technique for Treatment of Posttraumatic Bone Defects. *Sci. World J.* **2014**, *2014*, 710302. https://doi.org/10.1155/2014/710302.

(98) Kubik, J.; Aitken, S.; Buckley, R. Induced Membrane Technique for Bone Loss in the Lower Limb - Does the Masquelet Technique Work as Well as Its' Reputation Says It Does? *Injury* **2022**, *53* (2), 224–226. https://doi.org/10.1016/j.injury.2021.12.036.

(99) Warnke, P. H.; Bolte, H.; Schünemann, K.; Nitsche, T.; Sivananthan, S.; Sherry, E.; Douglas, T.; Wiltfang, J.; Becker, S. T. Endocultivation: Does Delayed Application of BMP Improve Intramuscular Heterotopic Bone Formation? *J. Cranio-Maxillo-fac. Surg. Off. Publ. Eur. Assoc. Cranio-Maxillo-fac. Surg.* **2010**, *38* (1), 54–59. https://doi.org/10.1016/j.jcms.2009.09.002.

(100) Betz, O. B.; Betz, V. M.; Nazarian, A.; Egermann, M.; Gerstenfeld, L. C.; Einhorn, T. A.; Vrahas, M. S.; Bouxsein, M. L.; Evans, C. H. Delayed Administration of Adenoviral BMP-2 Vector Improves the Formation of Bone in Osseous Defects. *Gene Ther.* **2007**, *14* (13), 1039–1044. https://doi.org/10.1038/sj.gt.3302956.

(101) Saito, N.; Okada, T.; Horiuchi, H.; Ota, H.; Takahashi, J.; Murakami, N.; Nawata, M.; Kojima, S.; Nozaki, K.; Takaoka, K. Local Bone Formation by Injection of Recombinant Human Bone Morphogenetic Protein-2 Contained in Polymer Carriers. *Bone* **2003**, *32* (4), 381–386. https://doi.org/10.1016/s8756-3282(03)00028-0.

(102) Xu, S.; Liu, J.; Zhang, L.; Yang, F.; Tang, P.; Wu, D. Effects of HAp and TCP in Constructing Tissue Engineering Scaffolds for Bone Repair. *J. Mater. Chem. B* **2017**, *5* (30), 6110–6118. https://doi.org/10.1039/C7TB00790F.

(103) Bose, S.; Fielding, G.; Tarafder, S.; Bandyopadhyay, A. Understanding of Dopant-Induced Osteogenesis and Angiogenesis in Calcium Phosphate Ceramics. *Trends Biotechnol.* **2013**, *31* (10), 594–605. https://doi.org/10.1016/j.tibtech.2013.06.005.

Appendices

Appendix A: 41% Vol hydroxyapatite slurry mixing protocol

Author: Katherine Lopez Ambrosio

Objective:

Production of 15ml of 41%Vol hydroxyapatite slurries suitable for 3D printing.

Reagents:

Name		Acronym	Quantity	Brand
Tricalcium phosphate tribasic (Hydroxyapatite)	Ceramic	HAp	19.311 g	Macron fine chemicals
Diphenyl (2,4,6trimethylbenzoyl) phosphine oxide	Photoinitiator	TPO	0.036g	TCI America.
Solplus D540	Dispersant	D540	1.46ml	Lubrizol Advanced Materials Inc.
Ethylene glycol dimethacrylate	Monomer	EGDMA	7.5ml	Scientific Polymer Products Inc.

Materials and equipment:

- ➢ [1] Stainless steel spatula.
- ➢ [2] Laboratory scoopula.
- ➢ [1] 1ml Luer tip syringe.
- ➢ [NA] Planetary ball mill (PBM) brand: across international.
- ➢ [10g] Agate balls (weight ratio 2:1 HAp to agate balls)
- ➢ [1] Teflon jar of 50ml for planetary ball mill with chemical resistant O-ring.
- ➢ [1] Measuring paper.
- ➢ [1] 10 ml Graduated cylinder.
- ➢ [1] Benchtop Balance.
- ➢ [NA] Parafilm film or tape.
- ➢ [10ml] Plastic syringe.
- ➢ [1] PTFE Syringe stopper.
- ➢ [NA] Aluminum foil.
- ➢ [1] Metallic tongs

Acknowledgments before beginning the procedure:

- Use protective glasses, gloves and lab coat.
- Use the fume hood for the mixing and transferring procedure.
- This procedure is to produce 15ml of HAp slurry. However, Due to the electrosteric interaction of the HAp particles with the dispersant, the resultant volume of slurry is lower.
- The planetary ball mill is in the factory campus. In the setting of this machine zero count a cycle. So, if we need 15min of mixing in a 50% duty cycle, the PBM is programmed to work 2 cycles and to rest 2 cycles.

Procedure:

1. Use the weigh paper, graduated cylinder and, 1ml syringe to measure the photoinitiator TPO, the monomer of EDGMA and dispersant D540 respectively. Add all to the Teflon jar.
2. Place 10g of agate media (5 big balls and approximately 6 small balls) in the Teflon jar.
3. Set the O-ring in the cleavage of the Teflon jar. Close and seal the jar and lid with parafilm paper.
4. Install and lock the jar in the PBM. Assure that the jar is completely fastened. Mix the components for 30 minutes at 120rpm in a 50% duty cycle (3 cycles 5 min on, 5 min off).
5. Wait until step 4 finishes.
6. weigh 10g of HAp.
7. Remove the jar from the PBM and add the HAp in the solution. Mix the components with the spatula and seal the jar and lid with parafilm.
8. Fasten the jar in the PBM and set it at 300RPM for 2h in a 50% duty cycle (12 cycles of 5min on, 5min off).
9. Wait until step 8 finishes.
10. Weigh 5g of HAp.
11. Repeat step 7.
12. Fasten the jar in the PBM and set it at 320RPM for 2h in a 50% duty cycle (12 cycles of 5min on, 5min off).
13. Wait until step 11 finishes.
14. Weigh 4.311g of HAp
15. Repeat step 7.
16. Fasten the jar in the PBM and set it at 360RPM for 4h in a 50% duty cycle (12 cycles of 5min on, 5min off).

Next day to transfer the slurry to the syringes.

17. Open the jar. Collect the agate balls with the tongs and clean the walls of the jar with the spatula.
18. Mix the slurry manually for 5min.
19. Assure visually that the slurry does not show any clusters of HAp and that it is homogenous. If it is not homogenous mix manually for 5min more.
20. Transfer the slurry to the plastic syringe, close the tip of the syringe with the stopper. Wrap the syringe with aluminum foil.

Appendix B: Scaffold/Sleeve Design Protocol

Sleeve/Scaffold Design Protocol

Author: Connor Witt

Last Edit: 6/2/2022

1. With Autodesk Fusion 360 open, disable the design history capture with the icon located in the bottom right corner of the screen
2. Under the "Mesh" tab, insert the imported DICOM data as an STL file
3. Once inserted, orient the STL file such that the proximal radius is parallel to the Z-axis and such that the center of the manus within the transverse plane is located right on the origin
4. Next, under the "Solid" tab, select the "Insert Canvas" button and insert the x-ray showing the osteotomy location as a canvas
   a. Orient the x-ray such that the proximal radius is parallel to the z-axis
   b. Next, using the calibrate function, calibrate the size of the x-ray and ensure that the dimensions of the imported DICOM data match the x-ray
   c. Once the dimensions of the imported STL are confirmed with the x-ray, orient the x-ray such that it matches the position of the STL file.
5. Then, using the proximal cut as indicated on the osteotomy x-ray, create a rectangle that is 1mm tall in the z direction and wide enough to intersect the ulna and radius. This step mimics the proximal cut performed during the osteotomy, and the resulting rectangle mimics the blade used during surgery.
   a. Then, using the "Combine" function located under the "Modify" section, perform a Boolean operation, and cut the STL file with the rectangle, ensuring no bodies are deleted in the process
   b. If the Boolean operation is unsuccessful, ensure there is clear contact between the rectangle and the proximal radius and ulna
6. Similarly, use the distal cut as indicated on the x-ray to create a 1mm tall (z direction) rectangle and perform steps 5a and 5b to mimic the surgical cut performed at the distal end of the radius.
   a. Multiple bodies may result from this operation due to the large number of facets located at the distal end of the radius, however, do not delete any bodies resulting from the operation
   b. This operation will require much time to calculate, so ensure the project has been saved prior to performing
7. Once the osteotomy has been performed, ensure the resulting defect has the correct dimensions as given by the x-ray.
8. Then, create a new sketch to create the cutting guide
   a. Create a sketch plane located at least 5mm away from the dorsal face of the manus

    b. Using straight lines, create a two-pronged shape, with the prongs of such fork aligning with the geometry of the second and fourth metacarpals, creating the distal "fork" of the cutting guide.

       i. Ensure that these prongs do not collide with the third metacarpal

      ii. The main body of the shape should align with the manus, but the most proximal edge of the main body should not collide with the distal radius

     iii. The main body should also encompass the distal rectangle as described in step 6

    c. On the same sketch plane, create a rectangle located at the proximal radius. This sketch will act as the proximal end of the cutting guide.

       i. This rectangle should fully encompass the radius and should be centered such that the proximal cut, as mentioned in step 5, is located at the center of the rectangle along the z-axis

      ii. The length of the rectangle along the z-axis should be approximately 50% the length of the defect along the axial plane

    d. Within the same sketch plane, create an additional rectangle that connects the two shapes mentioned in 8b and 8c. This connecting rectangle should encompass half of the ulna in the medial direction

9. Next, create one hole with a diameter of 1.75mm towards the distal end of each of the prongs as mentioned in section 8b.

10. Create another hole with a diameter of 1.75mm in the middle of the radius on the distal end of the portion. During surgery, k-wires are inserted into these holes to secure the cutting guide to the bone.

11. Then, extrude the sketches in the caudal direction such that there is clear contact between the proximal and distal ends of the cutting guide. The thickness of the proximal and distal ends of the cutting guide should be no less than 2mm but not larger than 20mm. The radius at the proximal end of the cutting guide should not be fully encompassed by the cutting guide, but should form a semi-circle

12. Then, using the rectangles that mimic the blade, as mentioned in 5 and 6, perform a Boolean operation to create the cuts needed in the guide for the surgeon to perform the cut.

13. Once the cutting guide has been created, import the fixation plate into the model and orient it such that lays in the same orientation as planned via surgery, allowing maximum contact between the proximal radius and the plate itself

14. Next, create a sketch plane located on the proximal end of the defect to start the design of the scaffold

    a. Using fit point splines, copy the shape of the radius and create an enclosed loop

    b. Then, on the most dorsal face of the sketch, add a rectangle that is 5mm wide by 1mm tall. This will act as the guide rail on the scaffold and helps secure the scaffold within the sleeve.

15. Similarly, create a sketch plane on the distal cut, located at the manus.

    a. Using fit point splines, copy the shape of the radius cut at this point.

b. The resulting shape should be larger than the sketch created at the proximal end of the defect, but should have a similar shape to the sketch created in step 14.
c. Likewise, on the most dorsal face of the sketch, add the 5 x 1mm rectangle to create the guide rail. This guide rail should be lay directly underneath the proximal rectangle in the Z direction

16. Once the two sketches for the scaffold have been created, use the "Loft" function under the "Create" tab to create the solid body
a. Make a copy of the resulting body and move this copy at least 50 mm away from the original
b. Then, using the "Scale" function under the "Modify" tab, scale the object down non-uniformly to 0.93 in both the X and Y directions
c. Then, on the distal and proximal faces of the scaled scaffold, create a 6 x 6 mm square oriented in the center of the face
d. Then, use the loft command with these two faces to cut the central canal of the scaffold
e. Then, using a sketch plane tangent to the rectangular guide rail, cut the scaffold into four parts of equal height with an interlocking pattern between the two central pieces. This interlocking pattern should have a stair step height of at least 10mm.
f. Add 5 mm to the distal end of the scaffold, and filet all edges within the scaffold.
g. Export the four scaffold pieces to STL with high refinement settings.

17. Using the scaffold that has not been scaled nor cut into four separate pieces, begin the design of the sleeve at the proximal end of the defect.
a. To do so, create a sketch plane on the proximal end of the defect after making the scaffold invisible. Then, move the sketch plane proximally by 20% of the defect length.
b. Create a 1.6 mm offset of the radius shape within the sketch.
c. Create a 1.0 mm offset of the fixation plate at that point.
d. Combine the two sketch objects with a fit point spline such that the resulting shape is an outline of both the plate and the scaffold and is self-contained
e. Repeat the offset process (steps 17b-17d) at the distal end of the scaffold and fixation plate.
f. Connect the resulting geometries with the loft command.

18. Once the sleeve is created as a solid body, use the "combine" function to perform a Boolean operation, with the scaffold, proximal radius, and the fixation plate as "cut" objects. The resulting sleeve should be hollow in the center, where the radius, scaffold, and fixation plate fit within.

19. Then, create three separate sketch planes tangent to the sleeve.
a. The first sketch plane falls opposite to the fixation plate, while the other two planes will fall tangent to the sleeve on opposite sides of the sagittal plane.
b. Utilize the "fit point spline" function to make a sinusoidal wave with half of a period and amplitude corresponding to the width of the sleeve on all three planes.

c. Create a second sinusoidal wave with the same dimensions as mentioned above, but 180 degrees out-of-phase with the first wave

d. Combine the objects such that the form a closed loop

e. Extrude all three sketches towards the sleeve and cut the sleeve to produce the permeability holes.

20. At the proximal end of the sleeve, create two holes with a diameter of 2.4 mm and tangent to the sleeve.

a. Ensure these holes occur in the upper 20% of the sleeve and, as such, collide with the proximal radius that is inserted into the sleeve

b. These holes must be offset in the z-direction such that the screws do not collide with one another when inserted into the radius

21. Once all of the dimensions have been verified, filet all edges within the sleeve such that no sharp edges are present

22. Export the sleeve and cutting guide as STL files with the default "high" refinment settings.

Appendix C: Guide for the Delivery and Day-of Preparation of the Device

Author: Adam Schneiderhan
Fall 2022
Colorado State University
Surgical Prep and Tech Workflow

The purpose of this document is to guide the two technicians who will be preparing the Prawel Lab endoprosthesis in the surgical suite/operating room, starting from the point at which all components of the device are dropped off at the CSU Veterinary Teaching Hospital (VTH) for sterilization (no less than one day prior to surgery, in the AM). These components are:

- Polycaprolactone (PCL) support sleeve
- Hydroxyapatite (HAp) tissue engineering (TE) scaffold (2-4 pieces, depending on the weight of patient)
- Polyethylene terephthalate glycol (PETG) surgical cutting guide
- PCL plate plugs (at least 15 per surgery)

The sterilization methods for each component are:

- **Sleeve**: Peracetic acid (PA) sterilization (2500ppm PA diluted with 20% ethanol)
- **TE Scaffold**: Autoclave (121°C, 2 atm, 20 min)
- Cutting Guide: Sterrad
- **Plugs**: PA sterilization

Preparing for the Operating Room (OR):

1. The two techs should be in communication with the surgeon and arrive to the VTH well before the scheduled surgery time.
2. Listen to the surgical staff for directions about where to proceed.
3. It is essential that you properly scrub, gown, and glove before beginning. **No components of the device should be touched with anything other than sterile, gloved hands.** Get formal training for how to scrub, glove, and gown *prior* to the day of surgery. Watch the following tutorials prior to training:
    a. [Tutorial for Hand Scrubbing](#)
    b. [Tutorial for Gowning and Gloving](#)

Preparing the device:

Once in the OR, the sterile components of the device will be available along with the following sterile instruments:

- Razor/scalpel
- Scissors
- Tweezers
- Sutures

If any of these are NOT available, notify a member of the surgical staff.

Step 1: Loading the sponge into the scaffold

1. Open the ¼" x 2" x 1" collagen sponge but *leave in the container until needed*.
2. On a sterile surface, cut the sponge lengthwise into four ¼" x ¼" x 2" pieces.
3. Acquire two different length of suture thread and tie one end of each thread to a piece of sponge.
4. Thread both suture threads through the central canal of the scaffold in the same direction.
5. Pull the shorter thread to pull the sponge through the central canal until it is flush with the far end.
6. Being careful not to move the previous sponge, pull the longer thread until the second sponge enters the central canal and meets the first sponge.
7. Cut the suture threads away with scissors, as well as any sponge* that sticks out from the ends of the scaffold and could cause the pieces to not meet.

*This is with the exception of the most proximal piece where the scaffold will meet the radius. In this case, we want the sponge to stick out and enter the medullary cavity of the radius.

8. Repeat steps 1-7 with each piece of scaffold. An example of this process can be seen here.

Note: The above video was not performed in a sterile environment and does not show the removal of excess sponge.

Step 2: Loading the scaffold with recombinant human bone morphogenetic protein (rhBMP)

1. Prepare the proper dosage of rhBMP using the Medtronic Infuse kit according to the manufacturer's protocol.
2. With the syringe loaded, insert the needle through the central canal of the scaffold, making sure not to push the sponge.

3. Steadily draw out the syringe while dispensing an even amount over the length of the sponge. Dispense an even fraction of the total volume into each scaffold piece (1/4 of the volume for 4 pieces, 1/3 for 3, etc.)

Step 3: Inserting the scaffold into the PCL Sleeve

1. Insert each piece of the scaffold into the distal end of the sleeve, starting with the most proximal piece and ending with the distal.
2. Make sure that each piece locks together and is in the proper orientation. The scaffold should end evenly with the distal end of the sleeve.

Step 4: Inserting plate plugs (Note: the surgeon may choose to perform this step themself).

At the surgeon's direction, use tweezers to push PCL plugs into the fixation plate holes that will be covering the TE scaffold

Appendix D: Manometer for the Calibration of Permeability Device Transducer

Source: https://www.validyne.com/blog/simple-manometer-calibrates-pressure-sensors/
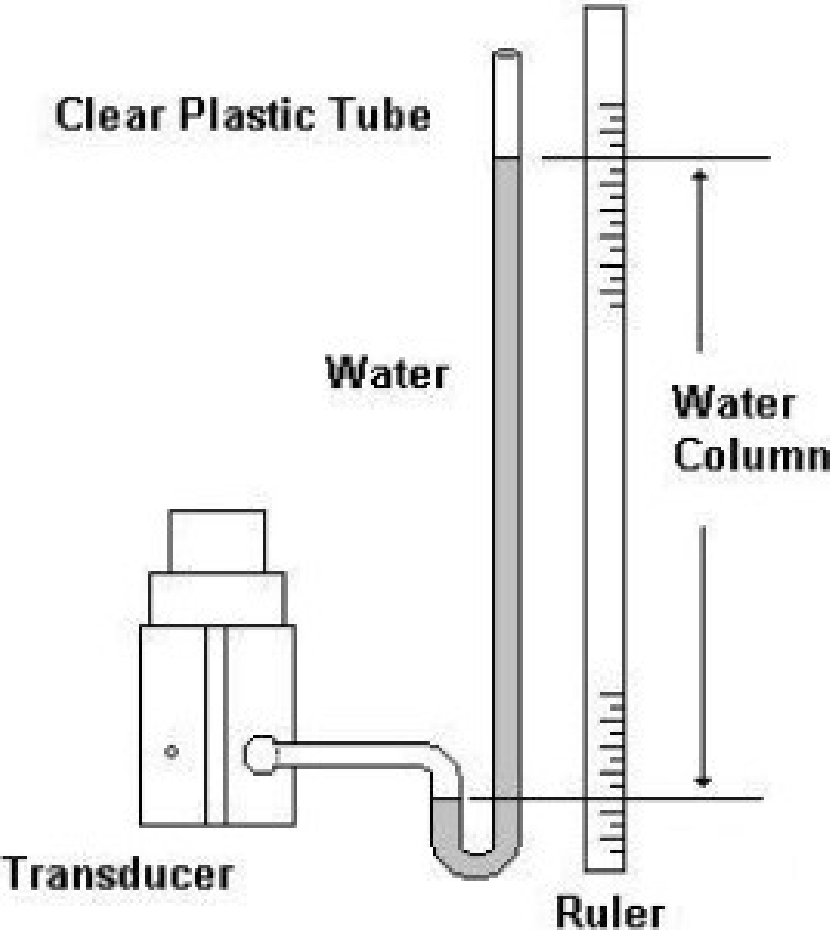
Appendix E: Surgical Component Modeling and Fabrication Workflow